Disorganized Inhibitory Dynamics and Functional Connectivity in Hippocampal area CA1 of 22q11.2 Deletion Mutant Mice

Stephanie A. Herrlinger[1,2,*], Bovey Y Rao[1,2,3,*], Margaret E. Conde Paredes[1,2,3,4], Anna L. Tuttman[1,2], Haroon Arain[1], Erdem Varol[4], Joseph A. Gogos[1,2,5,6,7], and Attila Losonczy[1,2]

[1] Department of Neuroscience, Columbia University, New York, NY, United States
[2] Mortimer B. Zuckerman Mind Brain Behavior Institute, Columbia University, New York, NY, United States
[3] Doctoral Program in Neurobiology and Behavior, Columbia University, New York, NY, United States
[4] Department of Computer Science & Engineering, Tandon School of Engineering, New York University, New York, NY, United States
[5] Department of Physiology, Columbia University, New York, NY, United States
[6] Department of Psychiatry, Columbia University, New York, NY, United States
[7] Stavros Niarchos Foundation Center for Precision Psychiatry and Mental Health, Columbia University, New York, NY, United States

Individuals with the 22q11.2 deletion syndrome, one of the strongest genetic risk factors for schizophrenia, demonstrate cognitive impairments such as episodic memory dysfunction. Place cell dynamics in the hippocampus supporting episodic memory are also impaired in a mouse model for the 22q11.2 deletion (*Df(16)A*$^{+/-}$). While hippocampal neural dynamics are under strong inhibitory control, there is no available information about functional alterations of molecularly identified inhibitory circuits in mouse models for the 22q11.2 deletion. Here, we examined interneuron subtype-specific activity dynamics in hippocampal area CA1 of *Df(16)A*$^{+/-}$ mice performing random foraging and goal-oriented reward learning tasks. We found that *Df(16)A*$^{+/-}$ inhibitory interneurons carry markedly reduced spatial information during random foraging. Mutant mice perseverate at rewarded locations during reward learning, and multiple interneuron types exhibit aberrant responses to reward locations. We observe task-dependent changes in functional correlation structure among multiple GABAergic subtypes, suggesting a broadly disorganized microcircuit functional connectivity in mutant mice. Overall, we identify widespread and heterogeneous subtype-specific alterations in interneuron dynamics during learning, depicting inhibitory microcircuits with impaired flexibility. Our study provides novel biological insights into how schizophrenia-risk mutations affect local-circuit interactions among diverse cell types in the mouse hippocampus during learning.

INTRODUCTION

Adults and children with the 22q11.2 deletion syndrome (22q11.2DS) demonstrate social and emotional impairments and an array of cognitive deficits[1,2]. 22q11.2 deletions are one of the strongest genetic risk factors for schizophrenia, resulting in a marked ~30-fold increase in the risk of developing the disease[1,3,4]. Cognitive deficits represent core features of schizophrenia and are likely mediated by the same abnormal physiological processes as more prototypical symptoms. Schizophrenia patients exhibit a spectrum of cognitive deficits, which are treatment-resistant and include relatively common and highly debilitating episodic memory dysfunction[5–7]. Episodic memory deficits represent the largest effect sizes among cognitive deficits[5], are often present prior to the onset of psychosis, and are frequently expressed in relatives of affected individuals[8–10].

While mouse models cannot completely capture all symptoms associated with a psychiatric disease, they can be used to model disease-associated mutations and assess core aspects of a disorder that may manifest in an equivalent manner in rodents[11–13]. Indeed, the employment of animal models of rare and highly penetrant risk mutations, coupled with core cognitive tasks and probed with high-resolution neuroscience techniques, has provided unprecedented expansion of our mechanistic understanding of mental illness. These approaches have introduced a new biological framework for studying psychiatric disease, focusing on the disordered activity and plasticity of both local and long-range neuronal assemblies and circuits[14–26]. These disruptions may suggest common points of convergence of genetic liability, leading to erratic neuronal activation patterns that trigger the constellation of cognitive symptoms and episodic memory deficits[12].

Hippocampal place cells, a subset of hippocampal principal cells that are selectively active in specific environmental locations, represent the cellular substrate of spatial and episodic memory[27,28]. Place cell ensembles are both sparse and dynamic[22,29–36], form rapidly in a novel context[37–39], and undergo experience-dependent stabilization as the environmental context transitions from novel to familiar[40–42]. Place cells also respond to salient reinforcers (e.g., reward)[22,30,43–46], and distinct, sparse populations of place cells represent different contexts[31,42,46–48]. A previous study uncovered behavioral and place cell correlates of episodic memory deficits associated with 22q11.2 deletions by employing a goal-oriented, hippocampal-dependent learning task in *Df(16)A*$^{+/-}$ mice, an animal model for the 22q11.2 deletion[22]. *Df(16)A*$^{+/-}$ mice showed a marked impairment in learning performance, which was disrupted by changes in task-context or reward location. Monitoring place cell activity dynamics during task performance revealed that place cells in hippocampal area CA1 exhibited reduced long-term stability, impaired context-related remapping, and a lack of reward-related reorganization.

These foundational observations offer an entry point to investigate microcircuit mechanisms by which schizophrenia risk mutations lead to altered hippocampal neural dynamics during learning. Nevertheless, the role of many circuit and cellular components critical for hippocampal neural dynamics has remained uncharacterized, representing a major gap in our knowledge of the biological cascades that drive disease-predisposing genetic lesions to clinical symptoms.

Inhibitory neurons, in particular, play a crucial role in shaping the activity of microcircuits in the brain by regulating the timing, amplitude, and synchronization of neuronal firing[49–51]. CA1 pyramidal cell activity and plasticity are under strong inhibitory control by a diverse array of GABAergic interneuron (IN) subtypes, each with distinct morphological, molecular, and functional properties[52–54]. Different subtypes of inhibitory neurons target specific subcellular compartments of excitatory neurons and exhibit specialized roles in regulating microcircuit function[53,55–60]. Dysfunction in inhibitory circuits has been implicated in numerous psychiatric conditions, most prominently in schizophrenia pathophysiology[19,20,61–70]. Therefore, understanding the role of inhibitory neurons in microcircuit dysfunction is essential for unraveling the complexity of neural networks and their contribution to various brain functions and disorders. Yet, the *in vivo* alterations of activity dynamics of most CA1 IN subtypes caused by 22q11.2 deletions remain completely unknown. As prior studies were limited to investigating IN subtypes in isolation ('one cell-type at a time'), a major barrier to identifying disease-associated inhibitory dysfunction has been the lack of holistic experimental and analytical approaches to examine functional interactions among multiple INs subtypes recorded simultaneously.

We recently developed large-scale simultaneous Ca^{2+} imaging and multiplexed molecular characterization of multiple GABAergic IN subtypes in the hippocampus[71,72]. Here we applied this approach in the hippocampal CA1 area of *Df(16)A*$^{+/-}$ mice and wild-type (WT) littermates to address major gaps in knowledge of the local circuit alterations associated with 22q11.2 deletion. Additionally, we newly developed a functional connectivity analysis to dissect the cellular components that contribute to the pathophysiology of schizophrenia-related memory deficits.

RESULTS

Interneuron subtype quantity or distribution in CA1 is unaltered in *Df(16)A*$^{+/-}$ mice.

To address these questions, we utilized an unbiased, large-scale, three-dimensional (3D) method for *in vivo* two-photon (2p) Ca^{2+} imaging of CA1 INs with random access acousto-optical deflector (3D-AOD) microscopy (Fig. 1)[71,72]. We performed 3D-AOD 2p Ca^{2+} imaging experiments on *Vgat-Cre::Df(16)A*$^{+/-}$ mice and WT littermates injected with a Cre-dependent adeno-associated virus for GCaMP7f expression in hippocampal area CA1 INs during a Random Foraging behavior paradigm (see methods, Fig. 1A,B)[71,72]. After taking a Z-stack of the dorsal CA1 field of view (Fig. 1C), we manually selected individual IN somas distributed across the 3D volume (Fig. 1D). 3D-AOD 2p Ca^{2+} imaging enables longitudinal monitoring of the simultaneous activity dynamics in large IN populations (up to ~250 cells per mouse) across all CA1 sublayers (Fig. 1E). We imaged these cells for two days while the head-fixed mice ran on a spatially enriched treadmill belt, navigating for randomly deposited water rewards. We performed *post hoc* immunohistochemical identification of imaged INs, manually registered them to their *in vivo* cell somas based on their GCaMP7f signal (Fig. 1F), and identified five major IN subtypes: axo-axonic cells (AACs), parvalbumin-expressing basket cells (PVBCs), somatostatin-expressing cells (SomCs), ivy/neurogliaform cells (IvC/NGFCs), and cholecystokinin (CCKCs) cells (Fig. 1G, see methods, Table 1)[52,53,59,71]. The subtype-specific distribution of imaged INs across CA1 sublayers was not noticeably altered in the mutants, and there were no significant differences in the number of IN

subtypes recorded per mouse or their proportional distribution within each CA1 layer (WT n=6 mice, 1127 total cells, 187.83 ± 15.22 cells per mouse; Df(16)A$^{+/-}$ n = 5, 775 total cells, 155 ± 30.21 cells per mouse)(Suppl. Fig. 1A-C). Using the markers from our subtyping strategy (see methods), we quantified the total number of Parvalbumin (PV+), Somatostatin (SST+), Neuropeptide Y (NPY+), Satb1+, and Cholecystokinin (CCK+) cells in CA1 and assessed labeled cell soma density by layer (Suppl. Fig. 1D-I). None of these quantifications illuminated differences in total cell numbers immuno-positive for each marker, consistent with previous findings in CA1 of other mouse models for this deletion[73].

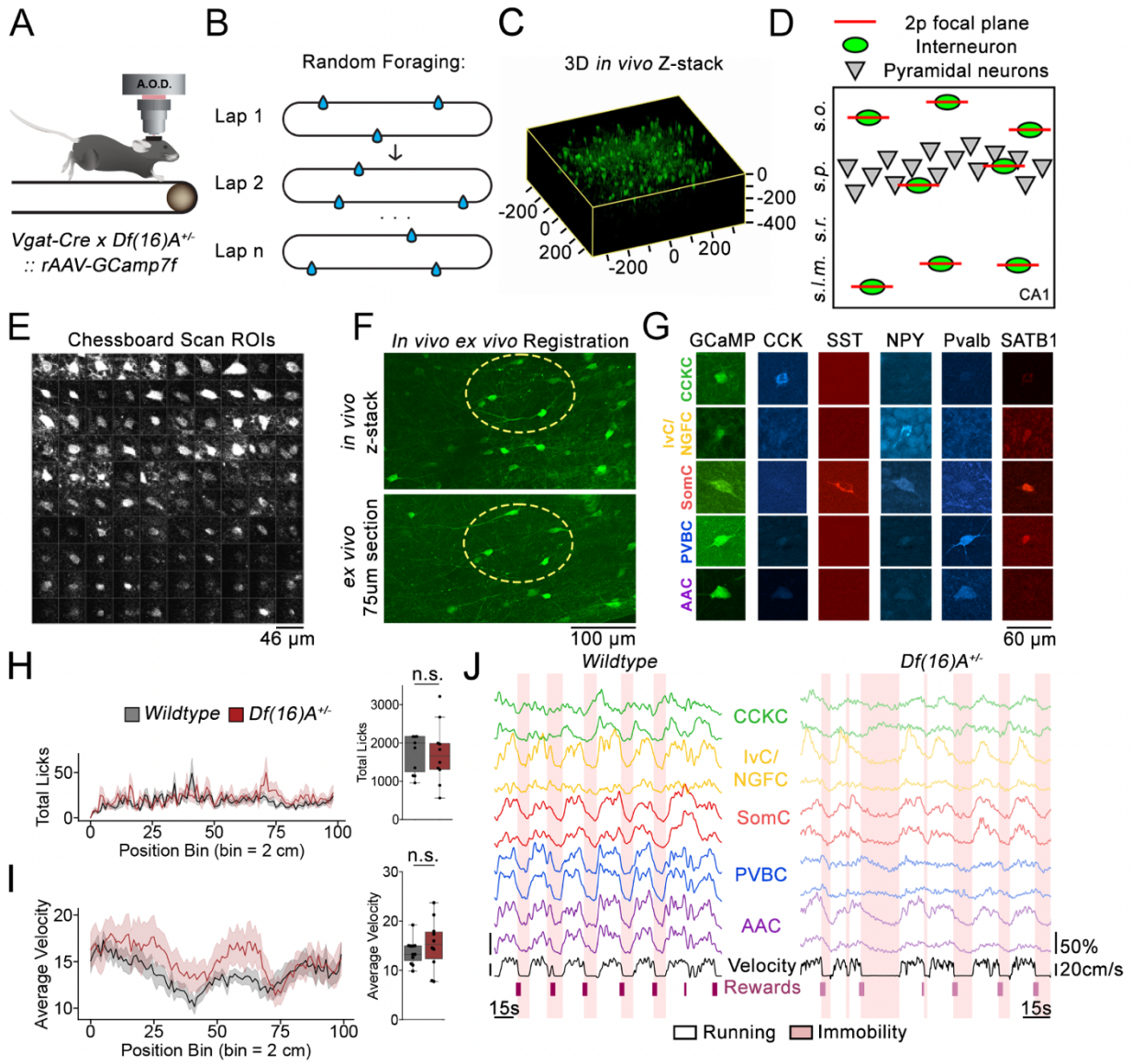

Figure 1. Interneuron subtype targeting strategy and imaging methodology. (A) Schematic of the *in vivo* imaging setup using acousto-optical deflector (*AOD*) microscopy and viral GCaMP7f expression strategy. *Vgat-Cre::Df(16)A$^{+/-}$* mice and WT littermates were injected with AAV1(*syn-FLEX-GCaMP7f*) in dorsal hippocampal area CA1 to express genetically encoded Ca^{2+} indicator, GCaMP7f in interneurons (INs) (B) Schematic of the Random Foraging behavior paradigm. Water-restricted mice were trained to run for randomly deposited water rewards across a 2-meter burlap belt with distinct features sewed across the belt. (C) 3-dimensional reconstruction of *in vivo* z-stack of INs in CA1. (D)

Schematic of the 3D imaging targeting strategy on the AOD, coronal view. *s.o.: stratum oriens, s.p.: stratum pyramidale, s.r.: stratum radiatum, s.l.m.: stratum lacunosum moleculare*. (E) Example time averages of the chessboard scan of 100 simultaneously imaged INs. *ROI*: regions of interest. (F) Example pair of *in vivo* and *ex vivo* images manually registered between imaging modalities. (G) Example images for each channel demonstrating the immunohistochemical (IHC) targeting strategy for IN cell-type characterization. Immunolabels are on the X-axis: *CCK*: cholecystokinin; *SST*: somatostatin; *NPY*: neuropeptide Y; *Pvalb*: parvalbumin. Cell-type labels used based on IHC strategy on the Y-axis: *AAC*: Axo-Axonic cells; *PVBC*: Parvalbumin Basket cell; *SomC*: Somatostatin-expressing cell; *IvC/NGFC*: Ivy/Neurogliaform cell; *CCKC*: Cholecystokinin-expressing cell. (H) Licking proportion of WT (black) and *Df(16)A*$^{+/-}$ (brown). There is no significant difference in lick location (left) or total licks (right) across the belt during Random Foraging in WT (n = 6) or *Df(16)A*$^{+/-}$ (n = 5) depicted by box-and-whisker plot, WT: 1534 ± 190 licks, *Df(16)A*$^{+/-}$: 1608 ± 291 licks, Welch's t-test, t = 0.208, p = 0.838. I) Average velocity plotted by location on the belt of WT (black) and *Df(16)A*$^{+/-}$ (brown) mice (left). There is no significant difference in average velocity during Random Foraging in WT (n = 6) or *Df(16)A*$^{+/-}$ (n = 5) depicted by box-and-whisker plot (right), WT: 13.7 ± 0.7 cm/s, *Df(16)A*$^{+/-}$: 15.2 ± 1.6 cm/s, Welch's t-test, t = 0.860, P = 0.405, ns = not significant. (J) Example relative GCaMP7f fluorescence ($\Delta F/F$) traces from molecularly identified interneurons during running and immobility bouts. WT Cell Numbers: AAC = 62 cells, SomC = 132 cells, PVBC = 46 cells, CCKC = 32 cells, IvC/NGFC = 73 cells; *Df(16)A*$^{+/-}$ cell numbers: AAC = 34 cells, SomC = 125 cells, PVBC = 51 cells, CCKC = 14 cells, IvC/NGFC = 47 cells. Boxplots show the 25th, 50th (median), and 75th quartile ranges, with the whiskers extending to 1.5 interquartile ranges below or above the 25th or 75th quartiles, respectively. Outliers are defined as values extending beyond the whisker ranges. *n.s.* = not significant.

Df(16)A$^{+/-}$ interneurons respond normally to locomotion

To assess *in vivo* functional activity dynamics of molecularly identified CA1 INs, *Vgat-Cre::Df(16)A*$^{+/-}$ mice and littermate WTs were water-restricted and taught to forage for water rewards distributed randomly on a spatially cued belt during 3D-AOD imaging (Fig. 1B). Licking and average running velocity were not different between *Df(16)A*$^{+/-}$ mice and WTs during this task (Fig. 1H,I). *Df(16)A*$^{+/-}$ mice also ran the same number of laps and did not exhibit obvious changes in belt occupancy (Suppl. Fig. 1A,B). Most INs exhibited strong, positive activity correlation with locomotion (Fig. 1J), which remained true in the described cell types in the mutant mice (Suppl. Fig. 1C)[71]. Similarly, CCKCs exhibited a bimodal correlation profile in both genotypes, with a subset of CCKCs showing negative velocity correlation[56,71]. Peri-stimulus time histogram analysis of subtype-specific IN activity during *Run-Start* and *Run-Stop* events showed no significant differences between genotypes (Suppl. Fig. 2D,E). Thus, locomotion-related activity dynamics of INs remain largely unaltered in mutant mice.

Df(16)A$^{+/-}$ interneurons represent reduced spatial information

We previously identified impaired place cell stability in CA1 and a trend for fewer place fields of place cells in mutant mice[22]. Place field formation and stability are under strong local inhibitory control[43,74,75], while a subset of INs themselves exhibit positive or negative place fields in WT mice[60,71,72,74,76,77]. To interrogate the contribution of inhibitory stabilization on circuit activity, we asked how well we could decode the mouse position during Random Foraging based on IN activity (Fig. 2A). We trained a support vector machine based on all recorded IN activity (see methods), and found a significant increase in decoding error in mutant mice INs. This deficit persisted even when corrected for the number of cells recorded per animal and the number of laps that mice ran (Fig. 2B,C). In addition, we also found a very near significant decrease in spatial information represented in mutant IN activity based on the Skaggs Information content (Fig. 2D)[78,79].

Next, we calculated spatial tuning curves for spatial selectivity in all IN subtypes during random foraging trials using the peak method (Fig. 2E)[71,80], and found that IN place field widths did not

differ between genotypes, and most place fields were detected under 30 bins of the track (Suppl. Fig. 3A). Overall, we detected fewer INs with place fields in *Df(16)A*$^{+/-}$ INs compared with controls (Fig. 2F). Interestingly, this deficit was enhanced when we removed cells that only exhibit negative place fields (Fig. 2G). As negative place cells alone were not reduced between genotypes (Suppl. Fig. 3B), this finding suggests a specific loss of positive place field information in mutant IN activity. When assessing all detected place field types altogether, a trend can be seen where *Df(16)A*$^{+/-}$ cells have fewer place fields per cell (Suppl. Fig. 3C). This deficit was more prominent when we again focused solely on positive place fields (Fig. 2H), suggesting a selective loss in positive place field enrichment in the mutant INs. When we examined which cell types may be contributing to this effect in the positive place field enrichment loss, AACs, PVBCs, and SomCs exhibited significant reductions in their positive place cell proportion, with a trend of decreased place preference in IvC/NGFC cells as well (Fig. 2I). Overall, fewer INs exhibit spatial selectivity in mutant mice (Fig. 2).

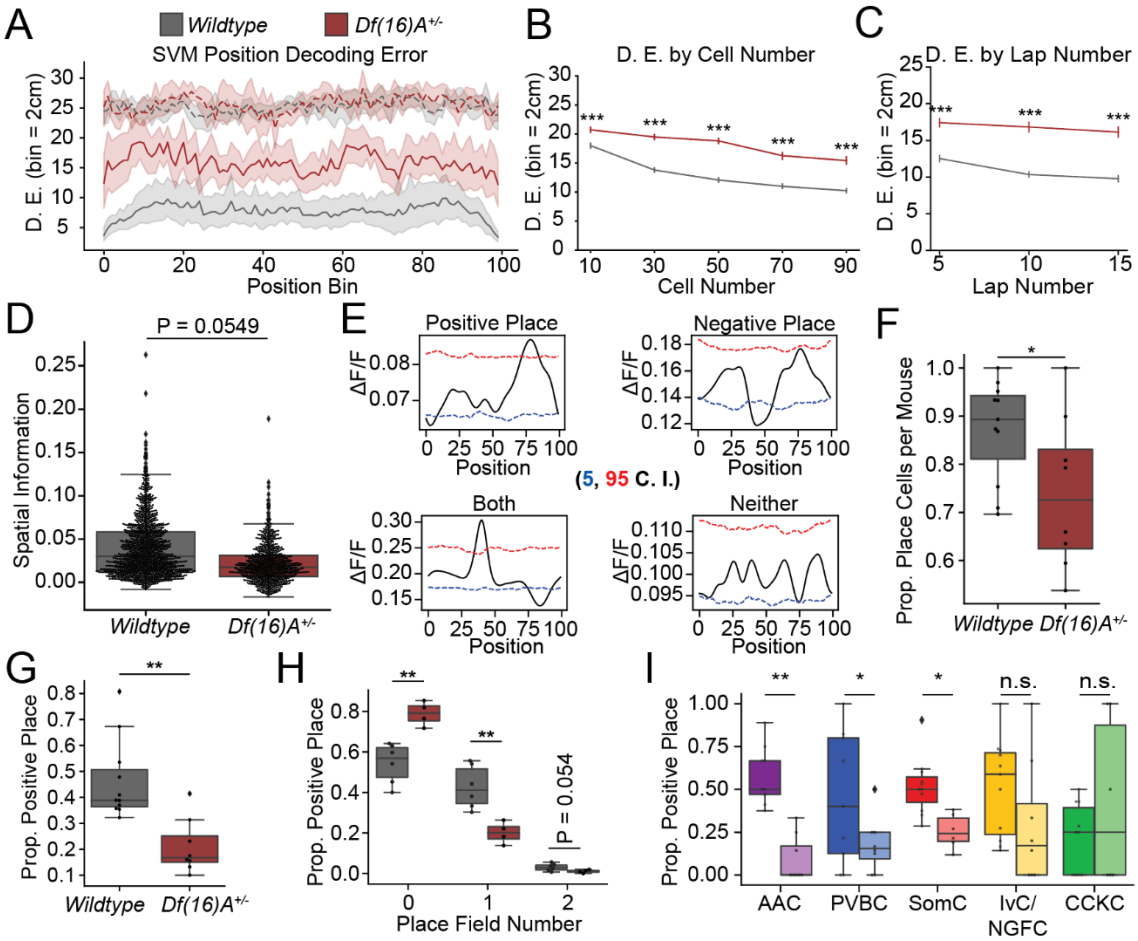

Figure 2: Reduced spatial information in Df(16)A$^{+/-}$ interneuron activity. (A) All recorded interneuron (IN) activity was used to train a support vector machine (*SVM*) to decode discrete position bins (*D.E.*: decoding error) across the belt. Each bin is equivalent to 2 cm. (WT: 16.4 ± 0.7 bins, n = 6; *Df(16)A*$^{+/-}$: 20.7 ± 0.9 bins, n = 5; Mann-Whitney U test: statistic = 0.0, P = 0.004). (B) SVM results iterated by number of cells used per genotype per bin (10 cells: WT: 18.0 ± 0.3 bins, *Df(16)A*$^{+/-}$: 20.7 ± 0.2 bins, Mann-Whitney U test: statistic = 2042, p = 2.48e-13, 30 cells: WT: 13.7 ± 0.7 bins, *Df(16)A*$^{+/-}$:19.5 ± 0.2 bins, Mann-Whitney U test: statistic = 115, p = 3.90e-33, 50 cells: WT: 12.1 ± 0.1 bins, *Df(16)A*$^{+/-}$: 18.8 ± 0.1 bins, Mann-Whitney U test: statistic = 47, p = 5.22e-34, 70 cells: WT: 11.0 ± 0.1 bins, *Df(16)A*$^{+/-}$: 16.3 ± 0.1

bins, Mann-Whitney U test: statistic = 16, p = 2.07e-34, 90 cells: WT: 10.2 ± 0.1 bins, *Df(16)A*$^{+/-}$: 15.4 ± 0.2 bins, Mann-Whitney U test: statistic = 244, p = 1.64e-31) (C) SVM results iterated by the number of laps used per genotype per bin. (5 laps: WT: 12.5 ± 0.1 bins, *Df(16)A*$^{+/-}$: 17.4 ± 0.2 bins, Mann-Whitney U test: statistic = 526.5, p = 4.12e-28, 10 laps: WT: 10.3 ± 0.1 bins, *Df(16)A*$^{+/-}$: 16.8 ± 0.2 bins, Mann-Whitney U test: statistic = 153, p = 1.18e-32, 15 laps: WT: 9.78 ± 0.1 bins, *Df(16)A*$^{+/-}$: 16.1 ± 0.2 bins,, Mann-Whitney U test: statistic = 41, p = 4.36e-34) (D) Skaggs information content of IN activity by genotype. (Comparison across animals: WT: 0.039 ± 0.005, n = 6; *Df(16)A*$^{+/-}$: 0.024 ± 0.006, n = 5; Mann Whitney U test: statistic = 4.0, P = 0.0549). Dots represent individual cell information content. (E) Example traces of positive place, negative place, both, and neither cells, based on the Peak Place method. Blue lines: lower bound to define significant negative place fields, red lines define significant C.I.: confidence interval. (F) Place field proportion between genotypes (WT: 0.87 ± 0.03, n = 11 trials across 6 mice; *Df(16)A*$^{+/-}$: 0.74 ± 0.06, n = 8 trials across 5 mice; Mann-Whitney U test: statistic = 22.5, P = 0.04). (G) Number of positive place fields detected per cell. *Df(16)A*$^{+/-}$ INs have fewer cells with positive place fields (WT: 0.46 ± 0.05, n = 11 trials across 6 mice; *Df(16)A*$^{+/-}$: 0.21 ± 0.04, n = 8 trials across 5 mice; Mann-Whitney U test (statistic = 7, P = 0.001)). (H) Number of positive place fields detected per cell. (0 fields: Mann-Whitney U test (statistic = 0.0, P = 0.0071), 1 field: Mann-Whitney U test (statistic = 0.0, P = 0.0071), 2 fields: Mann-Whitney U test (statistic = 4.0, P = 0.0549)). (I) Place field proportions by interneuron cell type. *AAC*: Axo-axonic cells Mann-Whitney U test: statistic = 0.0, P = 0.00027, *PVBC*: parvalbumin basket cells Mann-Whitney U test: statistic = 23.5, P = 0.122, *SomC*: Somatostatin-expressing cells Mann-Whitney U test: statistic = 5.0, P = 0.0028, *IvC/NGFC*: Ivy/Neurogliaform cells Mann-Whitney U test: statistic = 24.5, P = 0.058, *CCKC*: cholecystokinin cells Mann-Whitney U test: statistic = 24.5, P = 0.285. WT Cell Numbers: AAC = 62 cells, SomC = 132 cells, PVBC = 46 cells, CCKC = 32 cells, IvC/NGFC = 73 cells; *Df(16)A*$^{+/-}$ cell numbers: AAC = 34 cells, SomC = 125 cells, PVBC = 51 cells, CCKC = 14 cells, IvC/NGFC = 47 cells. Boxplots show the 25th, 50th (median), and 75th quartile ranges, with the whiskers extending to 1.5 interquartile ranges below or above the 25th or 75th quartiles, respectively. Outliers are defined as values extending beyond the whisker ranges.

Perseverant reward-related behavior in mutant mice

Next, we sought to interrogate inhibitory local circuit dynamics during a spatially guided reward learning task. For this, we trained the mice on a fixed reward task for 3 days prior to imaging with a non-operantly delivered reward (Fig. 3A). On the fourth day, CA1 IN Ca^{2+} activity was imaged during a 10-min trial in the familiar condition (Fig. 3B). On the second day of imaging, the location of the non-operant reward was translocated to the middle of the treadmill belt and repeated at that position on the third day (Reward Translocation task, Fig. 3B). Both genotypes learned this task well over the course of the three days, evidenced by increased licking leading up to and inside the reward zone during the three recording days (Fig. 3C). Mice displayed a quick adjustment to the translocated reward zone based on their licking behavior on the first translocation day (Fig. 3C, middle). Interestingly, we observed that mutant mice would lick more than their littermate counterparts overall (Fig. 3D), which appeared to be prominent at reward zones, suggesting that they were continuing to lick despite the discontinuation of the reward being delivered (after 2 seconds) (Fig. 3C). This phenotype did not appear to be an aspect of hyperactivity in this mouse line[81–83] as there was no difference in licking during the Random Foraging task (Fig. 1H). We additionally found that the mutant mice spent a greater proportion of time in the reward zones (Fig. 3E) despite running the same number of laps (Suppl. Fig. 4A) and having equivalent average speed (Suppl. Fig. 4B-E). Overall, mutant mice exhibited perseverant behavior at reward zones.

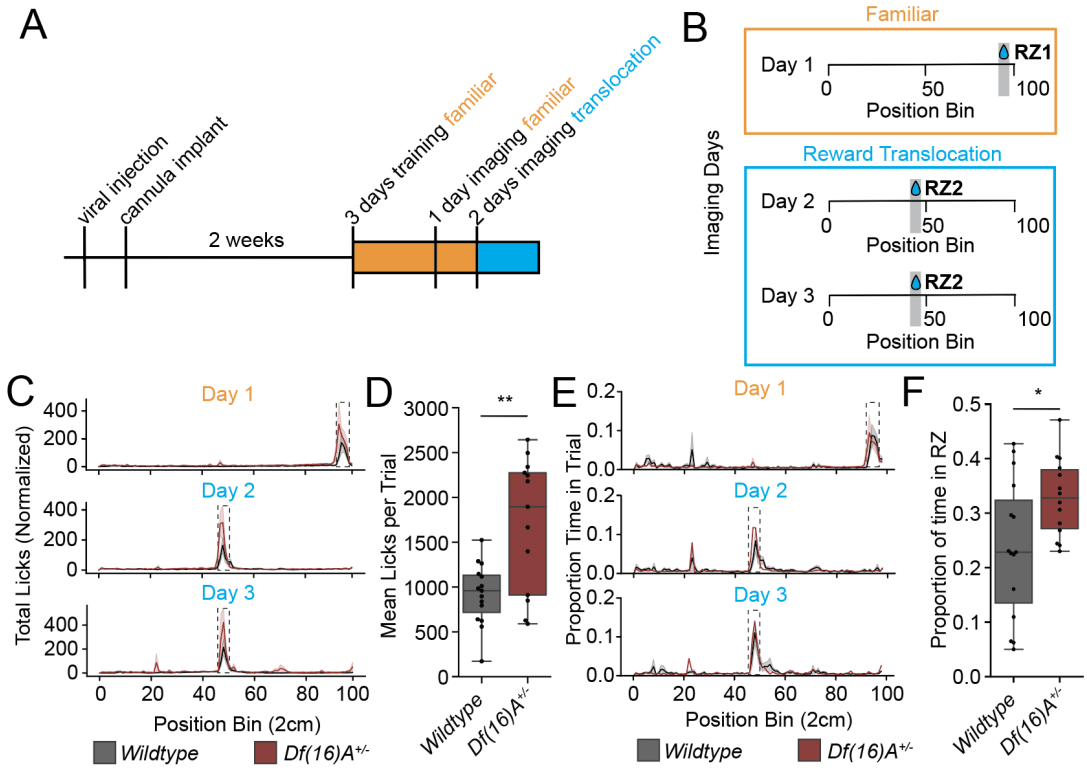

Figure 3. Mutant mice exhibit protracted reward response behavior. (A) Reward translocation task timeline schematic. Orange: familiar task trial days, Blue: reward translocation days. (B) Reward translocation task (*RZ*: reward zone) schematic for the three days of imaging, the familiar reward zone days (top), and the two reward translocation days (bottom). (C) Total lick distribution across position bins on familiar trial Day 1 (top), translocation Day 2 (middle) and translocation Day 3 (bottom) of recording. (D) Total licks across trials (WT: 921.07 ± 87.31 licks; *Df(16)A*$^{+/-}$: 1701.31 ± 206.53 licks; Mann-Whitney U test: statistic = 43, P = 0.0064). (E) Proportion of time spent across position bins on familiar trial Day 1 (top), translocation Day 2 (middle), and translocation Day 3 (bottom) of recording. (F) Proportion of time spent in the reward zone across trials (averaged across trials WT: 0.23 ± 0.03; *Df(16)A*$^{+/-}$: 0.328 ± 0.02; Mann-Whitney U test: statistic = 14, P = 0.02). *: $p < 0.05$. ***: $p < 0.00$. Boxplots show the 25th, 50th (median), and 75th quartile ranges, with the whiskers extending to 1.5 interquartile ranges below or above the 25th or 75th quartiles, respectively. Outliers are defined as values extending beyond the whisker ranges.

Subtype-specific alterations in reward-related inhibitory dynamics in *Df(16)A*$^{+/-}$ mice

Given that *Df(16)A*$^{+/-}$ mice display spatial learning deficits and decreased principal neuron enrichment near rewards[22,81] and altered reward-related behaviors (Fig. 3), we next aimed to characterize the reward-related activity of INs, which is known to be cell type-specific[71,84,85]. We hypothesized that there would be differential encoding of reward information in mutant mice compared to the littermate controls. First, to investigate direct inhibitory responses to reward, we examined neuronal activity of the IN subtypes during the random foraging task through reward-onset peristimulus time histograms (Fig. 4A, Suppl. Fig. 5A). We found that multiple INs subtypes displayed differential activity between genotypes during reward exposure as AACs, PVBCs, and SomCs showed a significantly higher response post-reward response (Fig. 4B). To interrogate reward-related inhibitory responses further, we next evaluated IN activity during the spatially guided Reward Translocation task (Fig. 4C, Suppl. Fig. 5D). Based on the averaged tuning curves around reward zones, we saw distinct reward-related activity of multiple IN subtypes between genotypes (Fig. 4D, Suppl. Fig. 5E). Intriguingly, there was a persistent activity of SomCs and

PVBCs preceding the old reward zone after the reward translocation on Day 2 (Fig. 4F,H). We also computed a reward zone modulation index (RMI) (as previously described,[71], by taking the signal prior to the *old* reward zone and normalizing it to the remainder of the belt. Here, we observed a similar effect where the RMI in the old reward zone revealed sustained SomC, PVBC, and IvC/NGFC activity in the mutant mice compared to the littermate controls after reward translocation (Fig. 4G,I,K). Using this measure, AACs uniquely showed aberrant reward-related activity only in active reward zones (Fig. 4D,J, Suppl. Fig. 5E,F), while IvC/NGFC show aberrant reward-related activity only after the reward has been translocated (Fig. 4J,K). While there was no significant difference in the number of place fields detected using the peak method during this task (Suppl. Fig. 5G), when we examined the spatial relationship of these fields with regard to reward by computing the distance of the center of each positive place field and the reward zone, we found that the positive IN place fields were significantly closer to the reward in mutant mice when compared to littermate controls (Fig. 4M). Furthermore, consistent with our observation from the Random Foraging task, there was still a significant decrease in spatial information represented in mutant IN activity during the Reward Translocation task (Fig. 4L) (based on the Skaggs Information content method,[79]. Therefore, the aberrant PVBC, AAC, and IvC/NGFC reward activity did not actually increase the overall spatial information retained from the belt while contributing to severely altered and persistent reward-related activity.

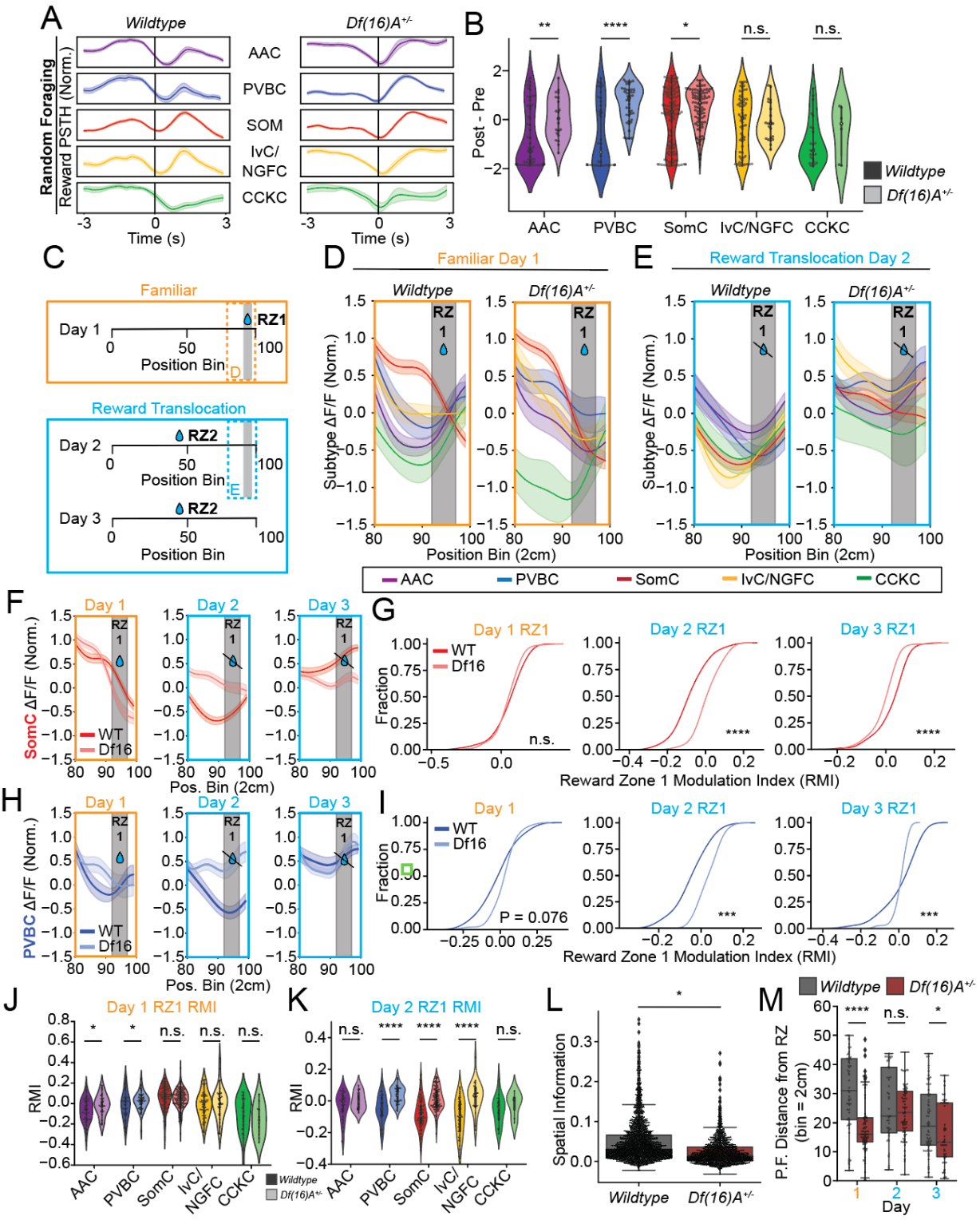

Figure 4. Aberrant subtype-specific activity during spatial reward learning task. (A) Averaged z-scored reward-onset peristimulus time histograms (PSTHs) by cell type across all cells within cell type during the Random Foraging task for 3 seconds pre- and 3 seconds post-stimulus. (B) Post - Pre PSTH responses per cell type before and after reward onset comparing the 3 seconds pre- to 3 seconds post-stimulus. *AAC*: axo-axonic cells Mann-Whitney U test: statistic = 344, P = 0.0017, *PVBC*: parvalbumin basket cells Mann-Whitney U test: statistic = 401, P = 1.45e-5, *SomC*:

Somatostatin-expressing cells Mann-Whitney U test: statistic = 4716, P = 0.012, *IvC/NGFC*: Ivy/Neurogliaform cells Mann-Whitney U test: statistic = 745.0, P = 0.492, *CCKC*: cholecystokinin cells Mann-Whitney U test: statistic = 67.0, P = 0.306 (C) Reward translocation task schematic. (D) Average responses of each cell type in the preceding 40 cm of the belt to the reward location in the WT (left) and *Df(16)A*$^{+/-}$ (right) on Day 1. (E) Average responses of each cell type in the preceding 40 cm of the belt to the prior reward location in the WT (left) and *Df(16)A*$^{+/-}$ (right) on Day 2 after reward translocation. (F) Average responses of SomCs in the preceding 40 cm of the belt to the old reward location in the WT (red) and *Df(16)A*$^{+/-}$ (pink) on all three recording days. (G) Reward zone modulation index (*RMI,* see methods under Reward Modulation Index) for SomCs at the old reward zone over three days. (Day 1: Kolmogorov-Smirnov (KS) test: statistic = 0.128, P = 0.282, Day 2: KS test: statistic = 0.526, P = 1.156e-11, Day 3: KS test: statistic = 0.399, P = 3.812e-6. (H) Average responses of PVBCs in the preceding 40 cm of the belt to the old reward location in the WT (dark blue) and *Df(16)A*$^{+/-}$ (light blue) on all three recording days. (I) RMI for PVBC cells at the old reward zone over three days. (Day 1: KS test: statistic = 0.277, P = 0.076, Day 2: KS test: statistic = 0.511, P = 2.055e-4 , Day 3: KS test: statistic = 0.471, P = 6.888e-4) (J) Reward modulation index in Reward Zone 1 on Day 1 per cell type. AAC: Mann-Whitney U test: statistic = 250, P = 0.175, PVBC: Mann-Whitney U test: statistic = 221, P = 2.052e-5, SomC: Mann-Whitney U test: statistic = 1661, P = 4.944e-12, IvC/NGFC: Mann-Whitney U test: statistic = 211, P = 4.35e-6, CCKC: Mann-Whitney U test: statistic = 44, P = 0.102 (K) Reward modulation index in Reward Zone 1 on Day 2 per cell type. AAC: Mann-Whitney U test: statistic = 250, P = 0.175, PVBC: Mann-Whitney U test: statistic = 221, P = 2.052e-5, SomC: Mann-Whitney U test: statistic = 1661, P = 4.944e-12, IvC/NGFC: Mann-Whitney U test: statistic = 211, P = 4.35e-6, CCKC: Mann-Whitney U test: statistic = 44, P = 0.102. (L) Skaggs information content of interneuron activity by genotype during the reward translocation task (WT: 0.058 ± 0.010; *Df(16)A*: 0.027 ± 0.005; Mann-Whitney U test: statistic = 5.0, P = 0.041). (M) Distance from the center of the detected positive place field (P.F.), surpassing the 95th percentile shuffle distribution) to the center of the reward zone. (Day 1: Mann Whitney U test: statistic = 1105.5, P = 2.327e-7, Day 2: Mann Whitney U test: statistic =1517.5, P = 0.172, Day 3: Mann Whitney U test: statistic = 1134, P = 0.010).

A probabilistic graphical model uncovers decreased inferred connectivity between interneuron subtypes in *Df(16)A*$^{+/-}$ mice

Neuronal cell-type is hypothesized as a key determinant of functional roles within neural circuits[56,71,86]. We sought to investigate whether neuronal identity can be accurately inferred from patterns of interactions among IN subtypes in local circuits of WT and mutant mice. We used a probabilistic graphical model (Fig. 5A, see methods) to quantify cell-specific functional correlations as variables within a hierarchical framework, encapsulating both individual cell-to-cell-type and broader cell-type-to-cell-type interactions. Utilizing this approach, we aimed to deduce molecular signatures of INs based on their interaction profiles with known IN subtypes and how these interaction profiles changed in mutant mice. This model captures the ensemble of interactions that a cell type typically engages in with the spectrum of other cell types within the circuit. The Bayesian inference process utilizes both the prior knowledge encoded in the model and the observed interactions to probabilistically assign cell types to the remaining cells in the circuit. The graphical representation of this model (Fig. 5A) illustrates the hierarchical nature of the model and the dependencies between the different levels of interaction.

The discernible clusters in the low dimensional projection of interaction parameters (Fig. 5B) suggest that our model captures salient features of cell interactions that facilitate cell type classification. To begin to probe cell-type activity relationships during behavior, we generated visualizations of the average cell-type interactions (Ω) to show the structural-functional correlations within the hippocampal network, notably recapitulating known mutual anticorrelated interactions such as CCKC-PVBC type INs during Random Foraging (Suppl. Fig. 6A, left) reported earlier[56,71,72]. Most cell type relationships tended to be more correlated than expected if their

activity was completely random during both tasks in WT mice (Suppl. Fig. 6A). Interestingly, when we compared the relative functional connectivity between genotypes, *Df(16)A*$^{+/-}$ showed a decreased correlation between IN subtypes when compared to the WTs, suggesting a microcircuit-wide perturbation of network activity in the mutant (Fig. 5C,D). The directionality of these changes is consistent between both behavior tasks with the exception of IvC/NGFCs, which show greater functional connectivity during the Random Foraging task and decreased functional connectivity during the Reward Translocation task, suggesting that this cell type may exhibit task-dependent changes in their network activity.

Our probabilistic model demonstrated robust classification for all five IN types tested (AACs, CCKCs, PVBCs, SomCs, IvC/NGFCs) in WT with accuracy significantly above random chance both during the Random Foraging (Fig. 5D, left) and the Reward Translocation tasks (Fig. 5D, center right). Interestingly, our results show both task-dependent and cell type-specific alterations in cell type predictability in *Df(16)A*$^{+/-}$ IN activity. During Random Foraging, neither AACs nor CCKCs were predictive, although the latter could be attributed to lower numbers of CCKCs recovered in the mutants (Fig. 5D, center left). Meanwhile, during the Reward Translocation task, while all cell types are still significantly predictive, both PVBCs and IvC/NGFCs become by approximately 25% more predictive based on their activity. This is expected for PVBCs, as we identified a reliable reward response only seen in the mutants, while this alteration in IvC/NGFCs again suggests a unique task-dependent functional change in their activity.

To examine these relationships with a separate analysis, we performed Pearson's cross-correlations analysis of cells to the average activity of a given cell class during a given trial. The CCKC category comprises both perisomatic-targeting basket cells (CCKBCs) and dendrite-targeting CCK+ INs[56,59,87]. CCKBCs are unique in their anticorrelation with velocity[56,71]. Therefore, as expected, we found that CCKCs in WT were the least correlated within-group and outside-group IN type characterized in this study (Suppl. Fig. 6, left). During Random Foraging, their activity exhibited a significantly increased in-group correlation in the mutants, suggesting that there may be a loss of distinct cell-type-specific activity within the CCKCs. In contrast, other cell-type comparisons trended towards an overall decrease in correlated activity, reflecting our previous separate analysis (Fig. 5C,D). In summary, our functional connectivity analysis based on probabilistic graphical modeling corroborated task-dependent alterations in relational activity between multiple IN subtypes, suggesting broadly disorganized microcircuit dynamics in mutant mice.

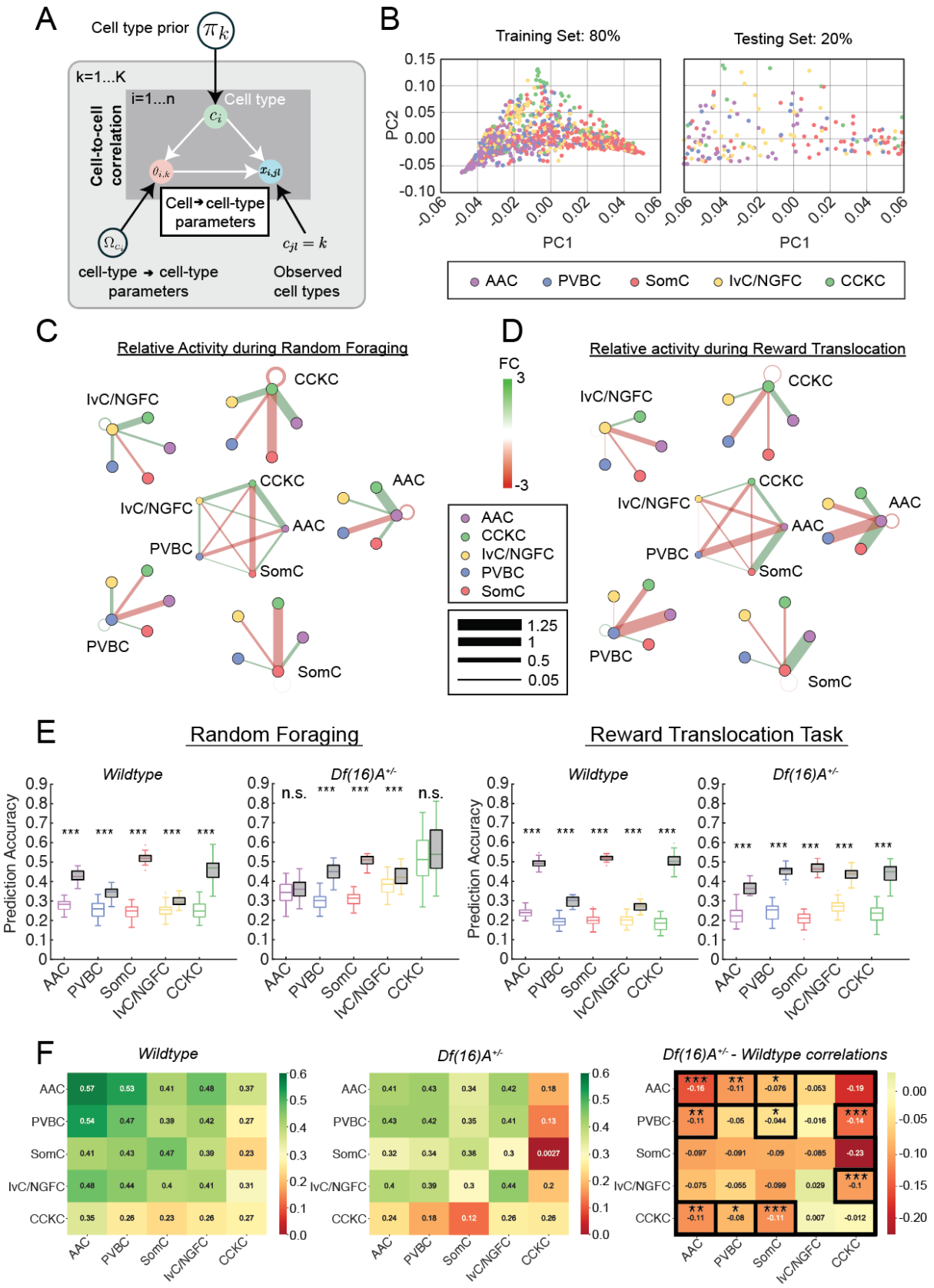
A
Cell type prior
k=1...K
i=1...n
Cell type
Cell-to-cell correlation
Cell→cell-type parameters
cell-type → cell-type parameters
Observed cell types
B
Training Set: 80%
Testing Set: 20%
PC1
PC2
AAC
PVBC
SomC
IvC/NGFC
CCKC
C
Relative Activity during Random Foraging
D
Relative activity during Reward Translocation
FC
E
Random Foraging
Reward Translocation Task
Wildtype
Df(16)A+/-
Prediction Accuracy
n.s.
F
Df(16)A+/- - Wildtype correlations

Figure 5: Functional connectivity alterations are dependent on brain state and genotype. (A) A schematic of the probabilistic graphical model of cell type-to-cell type interactions. The model begins with a cell type prior (π_k) for each of the K possible types denoting probability of assignment by chance. Each cell (i) is then probabilistically assigned a cell type (c_i) using maximum a posteriori estimation, weighed by the prior. Parameters $\theta_{i,k}$ reflect the unique interaction dynamics of cell i with cells of type k, and are derived from cell-to-cell correlations ($x_{i,j}$). These parameters are informed by both the observed cell types ($c_{ij} = k$) and the overarching cell-type-to-cell-type parameters (Ω_{ci}). See Probabilistic Graphical Model Framework section for more detail in methods section. (B) Left: projection of cell-to-cell-type interaction parameters ($\theta_{i,k}$) for all cells with cell types labeled in the training set. Cell types are denoted with the following colors: AAC (purple), CCKC (green), IvC/NGFC (blue), PVBC (yellow), and SomC (red). Right: projection of cell-to-cell-type interaction parameters ($\theta_{i,k}$) into a low-dimensional subspace for five different hippocampal IN subtypes in the testing set. (C,D) Circuit representation of the difference in cell-to-cell-type interactions between mutant *Df(16)(A)*$^{+/-}$ and WT genotypes by behavior paradigm (left: Random Foraging, right: reward translocation task), as determined by the probabilistic graphical model. Nodes represent different interneuron types, with colors corresponding to AAC (purple), CCKC (green), IvC/NGFC (blue), PVBC (yellow), and SomC (red). Edges connecting the nodes reflect the z-scores of the differences between the average correlations, with green edges indicating a correlation greater than expected by chance and red edges indicating less than expected. (E) Cell type classification accuracy using inferred cell types from *A* using our IN activity data for WT and *Df(16)(A)*$^{+/-}$ during Random Foraging (left) and reward translocation task (right). Light boxes indicate the null distribution of classification accuracy upon shuffling cell-type labels. *: P < 0.05, **: P < 0.01, ***: P < 0.001, n.s. not significant. P-values of WT for Random Foraging task: AAC (P = 3.48e-27***), PVBC (P = 3.91e-13***), SomC (P = 1.71e-43***), IvC/NGFC (P = 4.27e-07***), CCKC (p = 2.56e-23***). P-values of *Df(16)A*$^{+/-}$ for Random Foraging task: AAC (P = 3.94e-01, n.s.), PVBC (P = 1.47e-20***), SomC (P = 1.25e-32***), IvC/NGFC (P = 2.27e-04***), CCKC (P = 1.43e-01, n.s.). P-values of Wildtype for Reward Translocation Task: AAC (P = 8.76e-49***), PVBC (P = 1.58e-23***). SomC (P = 3.46e-53***). IvC/NGFC (P = 8.23e-15***). CCKC (P = 2.16e-40***). P-values of *Df(16)A*$^{+/-}$ for Reward Translocation Task: AAC (P = 2.52e-22***). PVBC (P = 7.21e-31***). SomC (P = 5.72e-41***). IvC/NGFC (P = 2.66e-29***). CCKC (P = 1.49e-24***). (F) Pairwise Pearson's correlation coefficient value matrix between cell types of ($\Delta F/F$) traces across the Reward Translocation trials from WT (left), *Df(16)A*$^{+/-}$ (center) and the comparative differences between genotypes (right). *: P < 0.05. **: P < 0.01. ***: P < 0.001. Boxplots show the 25th, 50th (median), and 75th quartile ranges, with the whiskers extending to 1.5 interquartile ranges below or above the 25th or 75th quartiles, respectively. Outliers are defined as values extending beyond the whisker ranges.

DISCUSSION

Our study provides the first comprehensive characterization of inhibitory local circuit dynamics in the murine hippocampus of mutant mice carrying a schizophrenia-predisposing genetic lesion. We found that mice carrying the 22q11.2 deletion, one of the strongest genetic risk factors for cognitive dysfunction and schizophrenia, exhibit broadly compromised hippocampal IN dynamics and functional connectivity. By examining IN subtype-specific responses during distinct spatial navigation tasks, our study uncovers distributed alterations at the microcircuit level that are represented more holistically and could only be captured incompletely by focusing on individual IN subtypes.

By monitoring IN activity dynamics during Random Foraging, we confirmed a strong correlation between IN activity and velocity during locomotion in *both* WT and *Df(16)A*$^{+/-}$ mice. Despite the relative conservation of these basic functional characteristics of hippocampal IN activity[55,56,58,71,88–90], our results also suggest a population-level deficit in the spatial information represented by INs in the *Df(16)A*$^{+/-}$ mice when compared to the WT littermates. Specifically, INs in the *Df(16)A*$^{+/-}$ mice carry significantly less spatial information (Figs. 2, 4), implicating a decrease in spatially localized inhibitory influence over CA1 pyramidal cell ensembles[71,75,91–95]. Interestingly, positive place field detection in INs was decreased while negative place fields were preserved, suggesting differential roles for dynamic IN activity.

Our study further identified alterations in the reward encoding of broad classes of INs within the *Df(16)A*$^{+/-}$ mice when compared to the WT littermates. Several studies have implicated the role of

specific IN subtypes in reward modulation, including SomCs and PVBCs[43,71,72,84,85]. Indeed, we identified PVBCs and SomCs as having particularly differential reward modulation during both random foraging and goal-oriented learning tasks, suggesting pervasive alterations in the hippocampal reward processing circuit. Previously, we found that *Df(16)A*$^{+/-}$ CA1 pyramidal neurons exhibit reduced reward zone enrichment during a goal-oriented learning task with a fixed reward zone, and that mice struggle to extinguish old reward zone location licking behavior compared to WT littermates[22]. Thus, these IN subtypes regulating the reward response may contribute to memory deficits and impaired reward-related representational dynamics of pyramidal cells observed in the *Df(16)A*$^{+/-}$ mice.

We identified large-scale relational networks of INs in *both* WT and *Df(16)A*$^{+/-}$ mice that revealed complex, inferred functional relationships between IN subtypes. We implemented a probabilistic graphical model of inferred connectivity, which revealed significant alterations in the relational activity of IN subtypes of *Df(16)A*$^{+/-}$ mice. We also found that by using the probabilistic graphical model of inferred connectivity, we could effectively predict several IN subtypes, underscoring a discernible pattern of interaction among cell types in the mouse hippocampus. However, the predictability of AACs and CCKCs during Random Foraging was not observed in *Df(16)A*$^{+/-}$ mice, suggesting a shift in the relational activity and a drift in the microcircuit activity. Our modeling approach paves the way for future investigations to expand on the structural correlates of functional connectivity patterns, potentially leading to a more comprehensive map of neural circuitry.

In the present study, we focused on major IN subtypes directly targeting pyramidal cells in CA1. Therefore, it remains to be determined whether the observed alterations in inhibitory subtype dynamics are drivers of disrupted pyramidal cell activity we previously reported[22] or, alternatively, these changes are a consequence of altered local recurrent or long-range excitatory inputs to INs[96–98]. Likewise, it will also be important to determine if disinhibitory circuits that inhibit other INs[43,71,99–101], including the subtypes investigated in the present study, also exhibit altered dynamics, perhaps playing a causal role in the observed alterations.

Studies in mouse models for schizophrenia and human patients insofar have predominantly focused on PV-expressing INs, implicating reduced prevalence and activity of these cells, which is associated with disorganized network activity[19,65,67,68,73,83,102–105]. Along these lines, destabilization in hippocampal neuronal dynamics analogous to the one described in Zaremba et al., 2017[22] has been subsequently recapitulated in hippocampal *in vitro* preparations from another model of the 22q11.2 deletion (*Lgdel/+* mice) and correlated with deficits in the synchronized activity of the CA1 neuronal network, in the form of diminished spike correlation between neuronal pairs and a reduction in neuronal oscillations in the theta frequency range[83]. Interestingly, these network deficits, as well as various hippocampal-dependent behavioral deficits, were partially or fully restored by acute pharmacological or chemogenetic manipulations of PV+ IN excitability, implicating inhibitory regulation in establishing stability of local circuit dynamics at least in the hippocampus. However, recent studies also implicate dysfunction in other IN types, including SomCs, Neuropeptide-Y-expressing INs and AACs in various disease-related cortical circuits[24,66,101,106–113]. Importantly, these subtypes directly interact with one another, with

implications for the functional output of the microcircuit. In agreement with this body of work, our results also show that PV+ INs deficits do not alone account for all IN deficits associated with this high schizophrenia risk locus. Diverse GABAergic INs express multiple genes encompassed within *Df(16)A* (Supp. Fig. 7A). The pattern of enrichment differs from the one observed for glutamatergic neurons, suggesting that distinct genetic pathways may be affected in glutamatergic and GABAergic cell types (Supp. Fig. 7B/C). Based on expression profiles, a network-wide genetic perturbation in INs could cause widespread dysfunction and altered excitation-inhibition balance rather than subtype-specific effects.

Overall, while further research is needed to fully elucidate the precise mechanisms by which 22q11.2 deletions and other risk mutations contribute to cognitive dysfunction and schizophrenia, it is increasingly evident that the effects are distributed across multiple IN subtypes within the brain, affecting how individual INs and ensembles of interacting IN cell types are engaged during cognitive operations in patients. Our findings suggest that genetic manipulation, modeling key aspects of schizophrenia risk such as 22q11.2 deletions, leads to changes in the functional connectivity of local IN ensembles that are markedly more pronounced than alterations in individual INs. This suggests that seemingly small functional changes in individual INs can lead to systems-level overt alterations when they are assembled into functional microcircuits.

Our study provides novel biological insights into how risk mutations predisposing to cognitive dysfunction and schizophrenia affect complex interactions among IN cell types in the mouse hippocampus during learning. Our work reveals a complex interplay between disease-predisposing genetic lesions, the brain's dynamic functional patterns, and, eventually, cognitive symptoms. The implications of this work also extend to the predictive modeling of neuron types based on their functional interactions, offering a novel approach to understand the complex interplay between the brain's molecular structure, its dynamic functional patterns, and how these patterns are altered under pathological conditions. Future investigations will aid in expanding the molecular and structural correlates of the observed altered IN activity and functional connectivity patterns, potentially leading to a more comprehensive understanding of how genetic liability leads to distorted maps of neural circuitry.

METHODS

RESOURCE AVAILABILITY

Lead Contact

Further information and requests for resources and reagents should be directed to and will be fulfilled by the lead contact, Attila Losonczy (al2856@columbia.edu).

Materials Availability

The study did not generate new unique reagents or mouse lines.

Data and Code Availability

Data and code reported in this paper are available from the lead contact upon request.

EXPERIMENTAL MODEL AND SUBJECT DETAILS

All experiments were conducted in accordance with NIH guidelines and with the approval of the Columbia University Institutional Animal Care and Use Committee. Experiments were performed with healthy, 2-5 month old, heterozygous adult male and female *Vgat-IRES-Cre* mice (Jackson Laboratory, Stock No: 016962, referred to as Vgat-Cre mice) that were crossed with hemizygous *Df(16)A*$^{+/-}$ mice generated as described [81]. Mice were held in a 12-hour light/dark cycle vivarium and housed 2-5 mice in each cage. All experiments were conducted during the light portion of the cycle. All mice used in the experiment were male (n = 11), with (n = 6 WT, n = 5 *Df(16)A*$^{+/-}$).

METHOD DETAILS

Viruses

Cre-dependent recombinant adeno-associated virus (rAAV) for GCaMP7f (rAAV1-syn-FLEX-jGCaMP7f-WPRE, Addgene #1944820-AAV1, titer: ≥1:10^{13} vg/mL) were used to express GCaMP7f in the hippocampus of *Vgat-Cre* mice. The Cre-dependent recombinase enabled expression of Ca^{2+} sensor GCaMP7f in Vgat+ interneurons (IN)).

Viral injections and hippocampal window/headpost implant

During isoflurane anesthesia, *Df(16)A*$^{+/-}$ Vgat-Cre mice were placed onto a stereotaxic surgery instrument. Meloxicam and bupivacaine were administered subcutaneously to reduce discomfort. The skin was cut along the midline to expose the skull and a craniotomy was performed over the right hemisphere with a dental drill. A Nanoject injector was loaded with a sterile glass capillary filled with mineral oil and rAAV1-syn-FLEX-jGCaMP7f-WPRE and lowered into dorsal CA1 of the right hemisphere. Injections were made at (in mm): AP -2.2, ML -1.75, DV - 1.8, -1.6, -1.4, -1.2, -1.1, -1.0, -0.8 relative to bregma with 64 nl of virus injected at each DV level. The pipette was held within the brain for 5-10 minutes after the last injection and slowly raised from the brain. The skin was sutured, and a topical antibiotic was applied to the suture site. Four days after viral injection, a circular cannula with a glass window was inserted into the cavity produced by craniotomy as previously described in ref. 96. Similarly, as described above, mice were anesthetized with isoflurane and placed on a stereotaxic surgery instrument. Meloxicam and bupivacaine were subcutaneously given to the mice. The skull was exposed, and a 3 mm

craniotomy was performed over the right hippocampus at AP -2.2, ML -1.75 relative to bregma, centered around the injection site. After removal of the dura, the cortex was slowly aspirated with negative pressure and the consistent application of ice-cold cortex buffer. When the horizontal fibers over CA1 were exposed, aspiration was stopped, and a sterile collagen membrane was applied to stop bleeding. A 3 mm circular cannula with a glass window was placed into the craniotomy and glued into the site with Vetbond. A headpost was then attached to the posterior of the skull with layers of dental cement. 1.0 mL of saline was subcutaneously given to each mouse, while the mice recovered in their home cage with a heat pad. All mice were monitored for 3 days of post-operative care until behavior training began.

Behavioral training and paradigms

Following the post-op recovery period, mice were acclimated to handling and head-fixation for a few days, while being water restricted to 85-90% of their original weight. Mice were trained to run on a fabric, cue-free belt with random rewards that were automatically dispensed at a decreasing number of random locations. Mice were trained for ~1 week on the cue-free belt and then were transitioned to the fixed reward task.

Random Foraging Task

Mice were imaged on a familiar context belt for 1 day with 3 random rewards distributed across the length of the belt, randomized every lap. On day 2 of imaging, a novel belt was introduced with the same random reward paradigm.

Reward Translocation Task

Mice were trained on a 2 m cue-rich belt with a fixed reward zone at the end of the belt for 3 or 4 days leading up to imaging. The belt consisted of four fabric ribbons with different textures and a variety of tactile cues: colored tape, foam strips, cotton pom poms, and etc. The following day the mice were imaged with the familiar reward zone location. On the second and third day of imaging, the reward zone was relocated to a new reward zone location at the center of the belt.

Two-photon Ca^{2+} imaging

After the mice were acclimated and trained in the respective tasks, a high-resolution structural Z-stack was captured 24 hours prior to imaging, while the mouse was anesthetized with isoflurane. The reference Z-stack was used to identify the 3D position of the GCaMP-positive neurons for access by the custom-modified AOD (acousto-optic deflector) microscope (Femto3D-ATLAS). The AOD microscope was used as previously described [71,72,74].

A water immersion objective (x16 Nikon CF175) was used to focus at the dorsal CA1 pyramidal layer and then fixed in position. A tunable two-photon laser (Coherent Ultra II) was adjusted to wavelength = 920 nm. The high-resolution structural Z-stack was captured in CA1 from ~100um below to glass to ~600 μm to span the entirety of CA1 from the *stratum oriens* to the *stratum lacunosum-moleculare* with a 800x800 pixel capture with a resolution of 1.25 μm per pixel with a 4 μm step size. Laser power and photomultiplier tube (PMT) detectors (GaAsP, H10770PA-40, Hamamatsu) were compensated in power and gain throughout the Z-stack capture. After the Z-

stack was completed, the mouse was returned to its home cage and given 24 hours to recover before functional imaging.

Using the integrated software from Femtonics (MES), the Z-stack was examined, and 100-150 INs were manually selected to generate a spreadsheet of the x-y-z positions at the center of each respective cell. These x-y-z positions served as the regions of interest (ROIs) that were then used on subsequent days by the AOD microscope to find the position of the corresponding interneurons. For each day of functional imaging in each mouse, the identical field of view was identified within the CA1 pyramidal layer, and then the ROIs were loaded using the software for AOD 3D imaging. Each imaging session was taken for 10 minutes, with 5-10 Hz for each recording experiment (frame rate depended on the number of ROIs, ROI size, imaging resolution, and scanning speed).

Immunohistochemistry

Mice were perfused with 20mL of Phosphate Buffered-Saline followed by 20 mL 4% paraformaldehyde (PFA, Electron Microscopy Sciences). The brains were stored in 4% PFA overnight and washed 3x5 min with PBS the next day. The brains were then sectioned for 75 μm transverse sections of the hippocampus on a vibratome and rinsed 3x15 min with PBS prior to immunohistochemical staining procedure. Histological tissue prep was performed as previously described[71,72]. In brief: sections were permeabilized 2x20 min with 0.3% Triton X-100 (Sigma-Aldrick), and subsequently blocked with 10% Normal Donkey Serum (Jackson ImmunoResearch) in PBST (PBS with 0.3% Triton X-100). After 45 minutes, the sections were incubated in PBS (containing 3 first-round primary antibodies, see below) for one hour at room temperature and then 2 days at 4°C with agitation. The sections were rinsed 3x15 min with PBS to wash out excess primary antibodies, and then, for two hours at room temperature, incubated in a PBS solution of secondary antibodies tagged for fluorescence (Table 1). Sections were then rinsed 5x15 min in PBS at room temperature and mounted onto rectangular glass slides with ThermoFisher Scientific aqueous mounting medium. After 1 hour of drying at 4°C, the slides were imaged. After imaging, PBS was used to remove coverslips, and sections were rinsed 3x15 min in PBS for round two of staining. The sections were blocked with 10% Normal Donkey Serum in PBST for 45 minutes before the addition of the round two primary antibodies. After, secondary staining protocol (now using round two secondary antibodies) was followed as completed in the first round. staining for CCK, SOM and NPY first led to stronger expression of fluorescence for those markers, opposed to staining for any of the three markers second (Table 1).

Antibody information and staining strategy

620

Cell Marker	Round	Primary Antibody (dilution)	Secondary Antibody (dilution)	Catalog #
Cholecystokinin (CCK)	1	rabbit anti-proCCK (1:500)	donkey anti-rabbit DyLight 405 (1:300)	Frontier Institute CCK-pro-Rb-Af350
Somatostatin (SST)	1	rat anti-somatostatin (1:500)	donkey anti-rat Alexa 568 (1:300)	Millipore MAB354
Neuropeptide-Y (NPY)	1	sheep anti-NPY (1:500)	donkey anti-sheep F(ab)2 Alexa 647 (1:300)	Abcam ab6173
Parvalbumin (Pvalb)	2	chicken anti-PV (1:5000)	donkey anti-chicken DyLight 405 (1:300)	*Gift from Susan Brenner-Morton*
SATB1	2	rabbit anti-SATB1 (1:1000)	donkey anti-rabbit Alexa 647 (1:300)	Abcam ab70004

Table 1

Assignment of subtype identity based on immunostaining

625 Interneuron subtypes were assigned based on our previously published classification strategy[71].

Axo-axonic cells (AACs):
Immunopositive for Pvalb and immunonegative for SATB1, SST, NPY, & CCK.

630 *Parvalbumin Basket Cells (PVBCs):*
Immunopositive for Pvalb and SATB1, immunonegative for SST, NPY, & CCK.

Somatostatin-expressing cells (SomCs):
Immunopositive for SST, with or without Neuropeptide Y (NPY) and SATB1, and immunonegative
635 for Pvalb and CCK.

Ivy / Neurogliaform cells (Ivy/NGFCs):
Immunopositive for Neuropeptide Y, with or without SATB1, and immunonegative for SST, Pvalb, and CCK.

640

Cholecystokinin-expressing cells (CCKCs):
Immunopositive for proCCK, immunonegative for SST, PV, NPY and SATB1.

Confocal imaging

645 The NikonA1 confocal microscope used to take multi-channel fluorescence images (405 nm, 488 nm, 561 nm, and 640 nm excitation for the four far-red, blue, green and red colored channels) of labeled tissue sections. Image capturing yielded 2048 x 2048 pixel z-stacks of the entire depth of the section (with 3 microns between each image of a given stack). Z-stacks were viewable via Fiji (Image J).

650

Registration of confocal images to *in vivo* z-stacks and identification of immunopositivity/negativity

Unique groupings of cells from *in vivo* z-stacks were used as visual fiducial markers to manually register *ex vivo* 75 μm z-stack images in ImageJ, section by section. Care was taken to note the orientation of the *ex vivo* sections with regard to the *in vivo* z-stack images. The coordinates taken from the AOD software when selecting ROIs for imaging against the *in vivo* z-stack were used to identify ROI ID numbers in the registered immunohistochemically stained images.

Immunohistochemical marker density quantification with CATT

A novel Cell Analysis/Typing Tool (CATT) designed by E.V., was used to identify positive cells in confocal fluorescence microscopy images. The code uses the entry of pixel dimensions to generate an image that combines the four fluorescence color channels of an original section. A region of interest (ROI) was drawn to delineate distinct CA1 layers for the program to focus on counting cells within a certain hippocampal layer. Given the ROI and pixel dimensions, the program outputs the volume, as well as an image displaying all of the IHC markers across the channels relative to the green channel (GCaMP7+ signal). Each positive cell marker was manually counted and divided by the ROI volume to derive positive marker density for a given ROI.

Behavior analysis

Licking behavior

For each animal during each experiment, the 2 meter belt was divided into 100 bins (~2cm per bin). The number of licks per bin per experiment were visualized to create licking curves. The proportion of licks that occur within the reward zone was also computed.

Reward zone occupancy and latency post-reward

Each animal's position per experiment was also digitized into 100 equal spatial bins representing the 2-meter belt. The occupancy time within the reward zone was quantified and compared between the genotypes. Furthermore, the time spent in the reward zone after the reward was no longer dispensed was computed and defined as the latency.

Imaging analysis

Pre-processing of Ca^{2+} imaging data

Raw movies of each individual cell were independently motion-corrected using the whole-frame cross-registration implemented in the SIMA package[116]. ROIs were then hand-drawn over each imaged cell. Fluorescence was extracted from each drawn ROI using SIMA. $\Delta F/F$ was then computed based on a 1st percentile baseline value over a 30-second rolling window. The $\Delta F/F$ traces were then smoothed using an exponential filter. For analyses involving velocity-regressed traces, each animal's velocity was smoothed with a Hanning filter, and then covariate linear regression was applied to each fluorescence trace where the smoothed velocity was regressed out.

Velocity correlation

For each cell, velocity correlation was computed by taking Pearson's correlation coefficient between the ΔF/F trace and animal's smoothed velocity with a -5 sec to +5 sec rolling lag. The highest absolute value of the correlation coefficients in this time window was taken as the correlation coefficient for the respective cell.

Run-Start/Run-Stop

Based on a velocity cut-off of 0.2 cm/s, run-start and run-stop events were observed throughout the imaging session. Each run-start and run-stop event was at least 10 imaging frames (1-2 seconds) and nearby events within 20 frames (3-5 seconds) were merged together. Peri-event time histograms were generated for each animal. The response magnitude for each cell was computed by taking the difference between the mean post-event ΔF/F and the mean pre-event ΔF/F.

Peri-Stimulus Time Histograms (PSTH)

For salient stimuli such as run-start/run-stop events and reward distribution events, a PSTH was constructed around each event respectively. These events were z-score and then averaged for each respective cell, and the z-scored averages were visualized using a heatmap or an averaged line-plot. A Post-Pre metric was calculated based on the z-scored averages as a measure for stimulus modulation.

Position decoding

A linear classifier support vector machine (SVM) was trained on the tuning curves of each respective cell, and the decoding error was visualized. The SVM was cross-validated by training the classifier on (n-1) laps and evaluating on the held-out lap, and this process was repeated such that every lap was utilized as a test lap at least once. Furthermore, the SVM was bootstrapped with different numbers of input cells and input laps averaged by animal to compare the position decoding efficacy between genotypes.

Spatial tuning curve

The 2-meter belt was divided into 100 bins (~2cm per bin). Spatial tuning curves for each cell during an experiment were generated by averaging the velocity regressed ΔF/F (as described above in preprocessing of Ca2+ imaging data) in each bin when the animal was running over 5 cm/s.

Peak place field calculation

The spatial tuning curves were shuffled 1000 times by circularly rotating the velocity-regressed ΔF/F tuning curves around the 100 spatial bins. Cells were classified as being spatially selective (i.e., having a place field) if the cell exceeded the 95th percentile (or was under the 5th percentile for negatively selective cells) with at least 10 sequential bins. The number of bins over or under the 95th and 5th percentile curves were visualized and a cutoff of 30 consecutive bins was used for the figures as it represented the approximate 75th quartile for place field width.

Spatial information

Using the spatial tuning curve, a spatial information score was computed following the methodology described by Skaggs et al 1992[79]. While the method was originally conceived for spiking data, we applied it onto the spatial tuning curve from Ca^{2+} data as a proxy for information content.

Reward Modulated Activity

For goal-directed experiments, the peri-event time histograms were constructed around each reward event. The 2-meter belt was divided into 100 bins (~2cm per bin). Tuning curves were generated by averaging the ΔF/F in each bin for both regular ΔF/F and velocity-regressed ΔF/F.

Reward Modulation Index

A reward modulation index (RMI) was computed as described in Geiller, Vancura et al., 2020[71,72]. Briefly, we compared the difference of the average activity 10 cm preceding the reward zone and the average activity on the remainder of the belt, normalized by the sum of the average activity over the two segments.

Cross-correlation analysis

Pairwise Pearson's correlation coefficients were computed for every pair of cells within a given experiment/trial. The average coefficient value for each subtype was then calculated per trial pair and averaged across mice.

Multivariate ridge regression analysis

A multivariate ridge regression model was trained on the ΔF/F trace of Ca^{2+} activity (velocity not regressed) for each cell with three predictors: velocity, position, licking. Each predictor was normalized to a 0-1 scale by using a minimum-maximum scaler. Given the inherent relationship between these variables, we used a ridge regression model with a cross-validated alpha value to limit the interaction between the predictors.

Probabilistic Graphical Model Framework

Model design

We designed a probabilistic graphical model to evaluate functional interactions between neurons, represented by the absolute correlation between any two cells i and j, denoted as $x_{i,j}$. Each cell i was associated with a cell type c_i, drawn from K distinct categories. The prior probability of cell i belonging to cell type k was represented by $p(c_i = k) = \pi_k$. For each experimental session, the recorded cells were randomly partitioned into two subsets: 80% were allocated to the training set and the remaining 20% to the test set. This split was performed to develop and assess the predictive model in a controlled manner. The labels for the test cells were concealed during the model training phase and were only revealed during the validation stage to verify the accuracy of the model's identification predictions.

Parameterization of cell interactions

Interactions between each cell and others of a given type k were modeled using a gamma distribution with parameters $\theta_{i,k}$, comprised of shape $\alpha_{i,k}$ and rate $\beta_{i,k}$. Here shape $\alpha_{i,k}$ and rate $\beta_{i,k}$

quantify how correlations between a cell of type k to individual cell i are distributed. For example, if all (or most) cells from type k is highly correlated with cell I both shape $\alpha_{i,k}$ and rate $\beta_{i,k}$ are going to be high values. Conversely, if most cells from cell type k do not interact with cell i, the shape parameter $\alpha_{i,k}$ is going to be close to 0. This parameterization was chosen to reflect the unique dynamics of interaction between cell i and cell type k, capturing the diversity and intensity of these inter-cell-type interactions and modeling the interactions as a random distribution to make the model fully Bayesian.

Multivariate distribution of interaction parameters

The full interaction profile of cell i across all K cell types was modeled using a multivariate Gaussian distribution, conditional on the cell type c_i. This distribution is defined by a mean vector μ_a and a covariance matrix Σ_a, specific to cell type a, and is denoted as $p(\theta_{i,1},...,\theta_{i,K}|c_i = a) \sim N(\Omega_a)$. This approach captures the ensemble of interactions that a cell of type a typically engages in with the spectrum of other cell types within the circuit.

Inference and Bayesian approach

We infer model parameters using Bayesian inference and computing the maximum a posteriori estimates of cell type c_i for a subset of cells $\{c_j\}_{j \in L}$, where L is the set of indices corresponding to known cell types. This process leveraged both the prior probabilities encoded in the model and the observed cell-to-cell interactions to probabilistically assign cell types to the remaining cells in the circuit. These analyses were performed for *Df16(A)*$^{+/-}$ and WT mice, separately.

Neuronal identity prediction

Classification validation

Our model was validated through its ability to classify cell identity based on functional correlation patterns. Model validation was performed by comparing the predictive accuracy of our probabilistic model against a null distribution. The null distribution was generated by shuffling cell type labels, thereby preserving the overall structure of the data while eliminating any true correlation between cell types and their functional interaction patterns. This approach allowed us to control for the possibility that any predictive success of the model could be due to chance. Predictive accuracies of our model were then contrasted with those from the null distribution to affirm the model's capability to identify cell types beyond random assignment. To assess the robustness of our probabilistic model, we conducted 31 independent runs, each initialized with a different random seed.

QUANTIFICATION AND STATISTICAL ANALYSIS

Statistical analyses

Subtype comparisons were conducted using one-way ANOVA tests with Tukey's range tests with correction for multiple testing if appropriate. For comparisons across genotypes, unpaired t tests were utilized if the data followed a normal distribution, assessed using the Shapiro-Wilk test. Otherwise, for non-normally distributed comparisons, the Mann-Whitney U test was used. The Kolmogorov–Smirnov test was used when comparing CDFs of continuous data. *: $P < 0.05$, **: P

< 0.01, ***: P < 0.001. All data analysis and visualization were done with custom software built on Python version 2.7.15, 3.8.11 and MATLAB R2023b.

Acknowledgements

S.A.H. is supported by the Burroughs Wellcome Fund. A.L. is supported by NIMHR01MH124047, NIMHR01MH124867, NINDSR01NS121106, NINDSU01NS115530, NINDSR01NS133381, NINDSR01NS131728, NIARF1AG080818. E.V. is supported by NIMHK99MH128772. J.A.G. is supported by NIMHR01MH124047 and NIMH R01MH097879. We thank Tristan Geiller, Bert Vancura for consultation on the analysis, and Erica Rodriguez for the mouse schematic in Fig. 1A.

Author Contributions

S.A.H., B.R., J.A.G., and A.L. conceived the study and wrote the manuscript. S.H. and B.R. performed experiments and analyzed the data with assistance from M.E.C.P., A.T., and H.A.. S.H. and E.V. conceived the connectivity and CATT analyses, which was developed and implemented by E.V., M.E.C.P., and H.A.

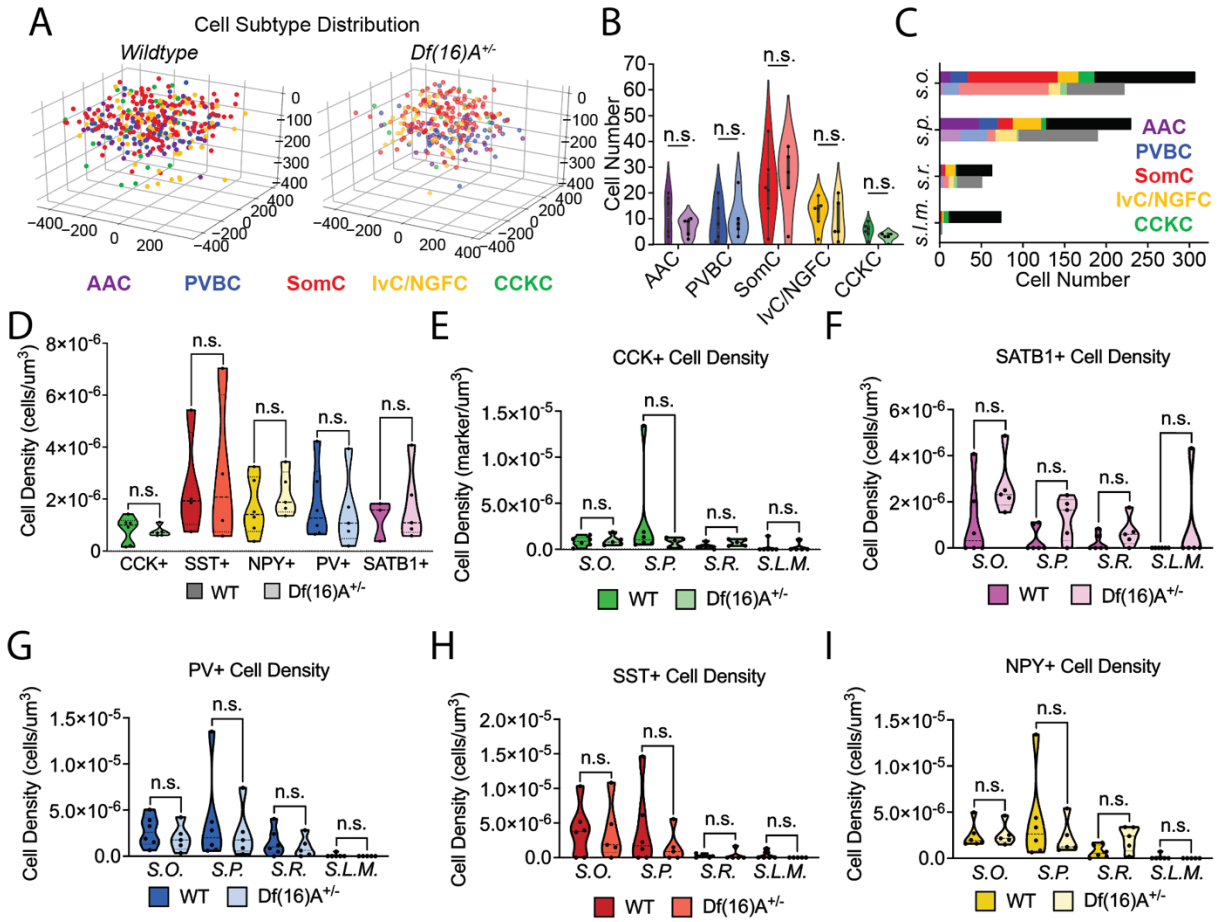

Supplemental Figure 1. 3D-AOD imaging and molecular characterization strategy for interneuron subtypes. (A) Summary distribution plots of all cells imaged in this study for each genotype based on imaging coordinates superimposed across all animals (n = 6 WT, n = 6 *Df(16)A*$^{+/-}$ mice). (B) Cell type number totals averaged per genotype (n = 6 WT, *n* = 5 *Df(16)A*$^{+/-}$ mice). (C) Distribution of total cells identified, ordered by cell type, across all layers of CA1. *s.l.m.: stratum lacunosum moleculare; s.r.: stratum radiatum; s.p.: stratum pyramidale; s.o.: stratum oriens.* (D) Quantification of total marker density for all immunohistochemical markers used (unpaired t-tests with Welch's correction (P > 0.05)).(G) Quantification of the density of parvalbumin+ cells within each layer of CA1. *PV*: parvalbumin. 6-7 serial 75 μm sections were stained and quantified for PV+/GCaMP+ cell signal across the four layers of CA1 in n = 6 WT, n = 6 *Df(16)A*$^{+/-}$ mice (unpaired t-tests with Welch's correction (P > 0.05)). (H) Quantification of the density of somatostatin+ (*Som*) cells within each layer of CA1. 6-7 serial 75 μm sections were stained and quantified for Som+/GCaMP+ cell signal across the four layers of CA1 in n = 6 WT n = 5 *Df(16)A*$^{+/-}$ mice (unpaired t-tests with Welch's correction (P > 0.05)). (I) Quantification of the density of NPY+ cells within each layer of CA1. 6-7 serial 75 μm sections were stained and quantified NPY+/GCaMP+ cell signal across the four layers of CA1 in n = 6 WT, n = 6 *Df(16)A*$^{+/-}$ mice (unpaired t-tests with Welch's correction (P > 0.05)). *NPY*: Neuropeptide Y. (J) Quantification of the density of SATB1+ cells within each layer of CA1. 6-7 serial 75 μm sections were stained and quantified for SATB1+/GCaMP+ cell signal across the four layers of CA1 in n = 6 WT, n = 6 *Df(16)A*$^{+/-}$ mice (unpaired t-tests with Welch's correction (P > 0.05)). (K) Quantification of the density of cholecystokinin+ cells within each layer of CA1. *CCK*: Cholecystokinin. 6-7 serial 75 μm sections were stained and quantified for CCK+/GCaMP+ cell signal across the four layers of CA1 in n = 6 WT n = 6 *Df(16)A*$^{+/-}$ mice (unpaired t-tests with Welch's correction (P > 0.05)). *n.s.*= not significant.

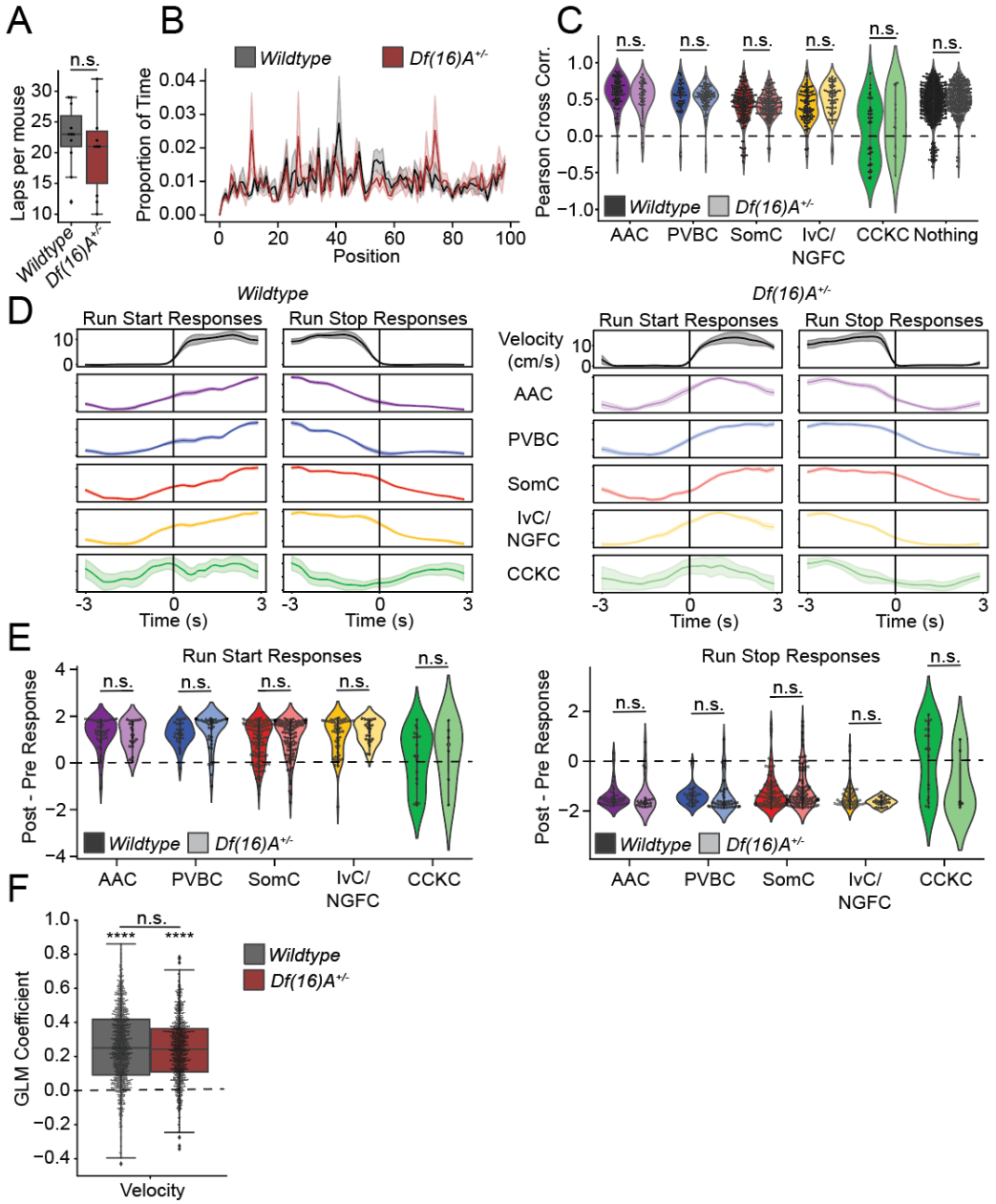

Supplemental Figure 2. No changes in locomotion-related activity. (A) Total laps across mice within genotype (WT: 22.6 ± 1.5 laps, *Df(16)A*$^{+/-}$: 20.6 ± 2.2 laps, Welch's t test, t = 0.74, P = 0.47). (B) Average percent occupancy on the belt by position per genotype (Mann-Whitney U test, statistic = 4695.5, P = 0.3). (C) Pearson correlation coefficients of interneuron activity and velocity for all tested interneuron subtypes (WT: n = 97 AACs, 53 PVBCs, 194 SomCs, 115 IvCs/NGFCs, and 44 CCKCs from n = 6 mice, *Df(16)A*$^{+/-}$: 46 AACs, 87 PVBCs, 181 SomCs, 72 IvCs/NGFCs, and 14 CCKCs from n = 5 mice). WT: one-way ANOVA ($p < 10^{26}$), *Df(16)A*$^{+/-}$: one-way ANOVA ($P < 10^{10}$) with post hoc Tukey's range test corrected for multiple testing. (D) Peristimulus time histograms (PSTHs) of average traces during Run-Start and Run-Stop events, Left: WT, Right: *Df(16)A*$^{+/-}$. (E) Average Post-Pre PSTH responses to Run-Start (Left) and Run-Stop (Right) events. (F) Ridge Regression Model shows velocity as a significant predictor of IN GCaMP-Ca^{2+} activity. Wilcoxon: WT: 0.257 ± 0.007, statistic = 21129.0, P = 4.68e-141, *Df(16)A*$^{+/-}$: 0.240 ± 0.007, statistic = 11194.0, P = 3.60e-117. Boxplots show the 25th, 50th (median), and 75th quartile ranges, with the whiskers extending to 1.5 interquartile ranges below or above the 25th or 75th quartiles, respectively. Outliers are defined as values extending beyond the whisker ranges. *n.s.* = not significant.

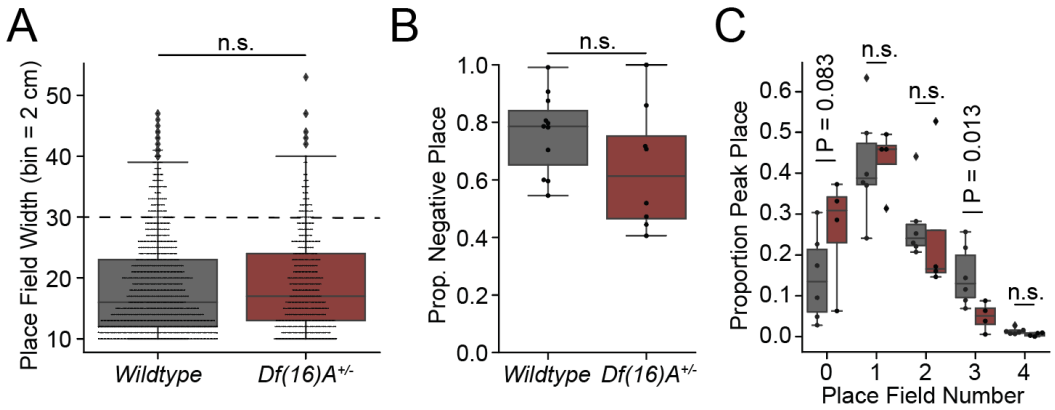

Supplemental Figure 3: Negative place fields are not reduced in *Df(16)A*$^{+/-}$ compared with WT. (A) Positive place field widths of detected place fields using Peak Place method. Averaged across animals: Mann-Whitney U test (statistic = 14.0, P = 0.464). (B) Negative place fields detected between genotypes. WT: 0.76 ± 0.04, *Df(16)A*$^{+/-}$: 0.64 ± 0.08 Mann-Whitney U test (statistic = 27, P = 0.087). (C) Number of all detected place fields per cell by genotype. 0 place fields: Mann-Whitney U test (statistic = 5.0, P = 0.0829), 1 place field: Mann-Whitney U test (statistic = 11.0, P = 0.4576), 2 place fields: Mann-Whitney U test (statistic = 6.0, P = 0.1205), 3 place fields: Mann-Whitney U test (statistic = 1.0, P = 0.0126), 4 place fields: Mann-Whitney U test (statistic = 4.0, P = 0.0549). Boxplots show the 25th, 50th (median), and 75th quartile ranges, with the whiskers extending to 1.5 interquartile ranges below or above the 25th or 75th quartiles, respectively. Outliers are defined as values extending beyond the whisker ranges. *n.s.* = not significant.

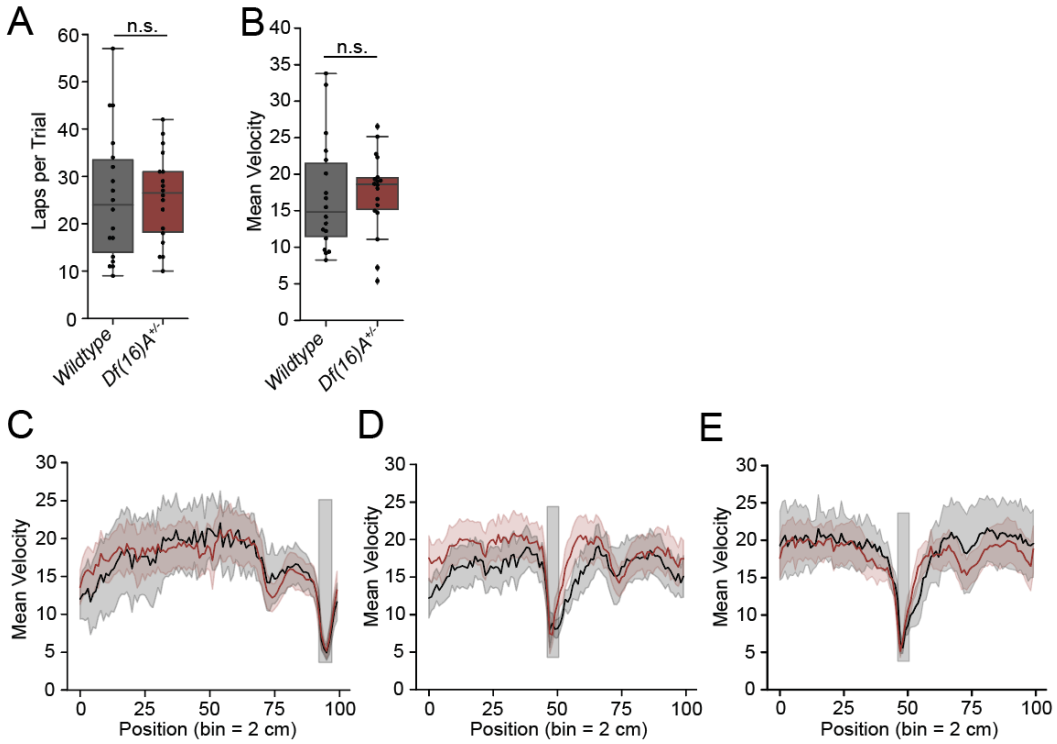

895 **Supplemental Figure 4: Additional data on mouse behavioral performance.** (A) Average laps run by mouse per trial Averaged across animals (WT: 25.72 ± 3.16 laps; *Df(16)A*$^{+/-}$: 25.66 ± 2.16 laps; Mann-Whitney U test: statistic = 151, P = 0.37). (B) Average laps run by mouse per trial **(**Averaged across animals: WT: 17.02 ± 1.82 laps; Df(16)A$^{+/-}$: 17.49 ± 1.30 laps; Mann-Whitney U test: statistic = 139, P = 0.24). (C-E) Average velocity by position on the belt for Day 1 (C), Day 2 after translocation of the reward (D), and Day 3 (E). *n.s.* = not significant.

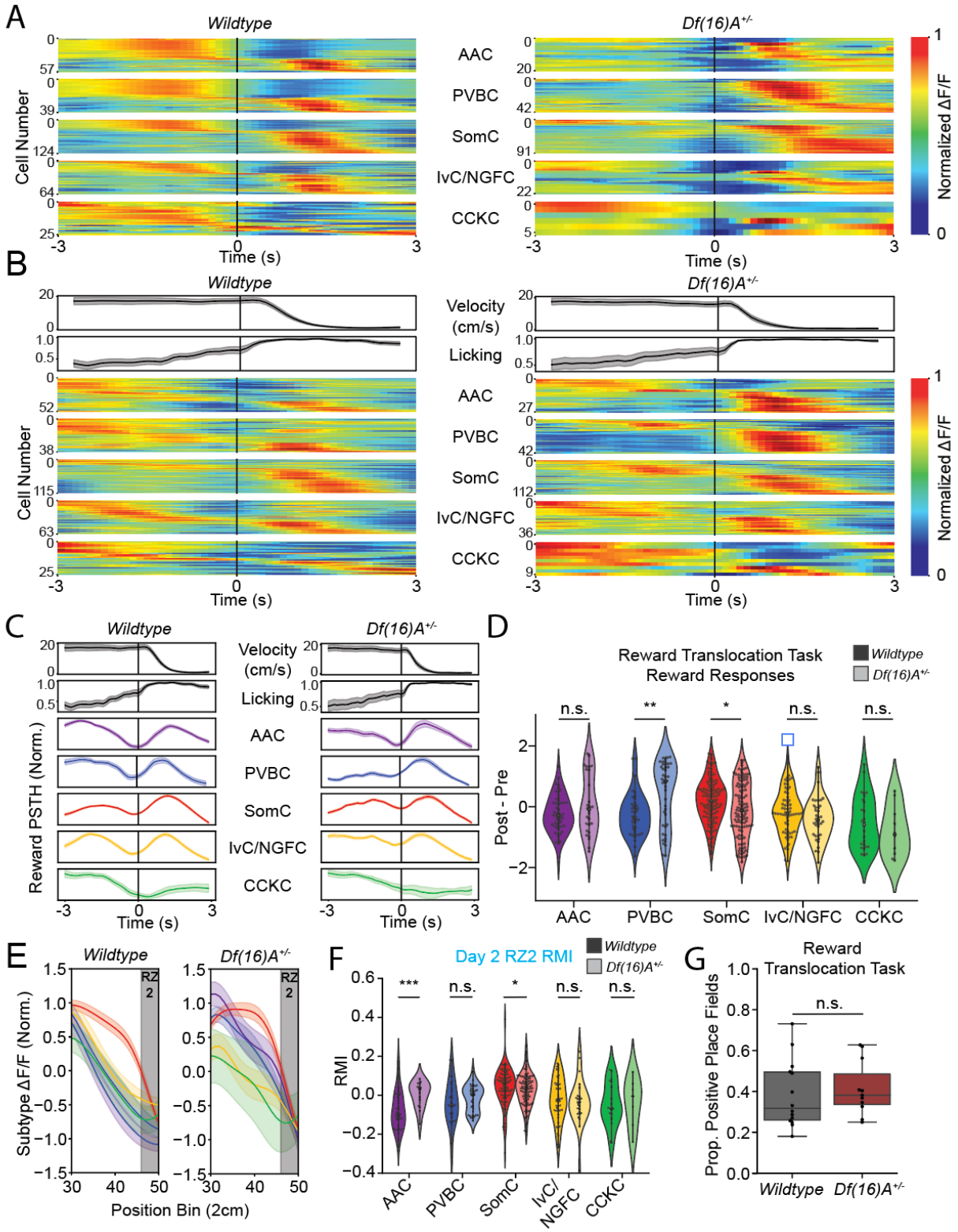

900 **Supplemental Figure 5: Reward Modulation alterations.** (A) Individual cell responses to reward during random foraging task, Left: WT, Right: *Df(16)A*$^{+/-}$ (B) Individual cell responses to reward during reward translocation task, Left: WT, Right: *Df(16)A*$^{+/-}$ (C) Average cell responses to reward during reward translocation task, Left: WT, Right: *Df(16)A*$^{+/-}$ (D) Post - Pre cell responses centered around the reward onset for reward translocation task. AAC: Mann-Whitney U

test: statistic = 631, P = 0.136, PVBC: Mann-Whitney U test: statistic = 524, P = 0.002, SomC: Mann-Whitney U test: statistic = 5464, P = 0.015, IvC/NGFC: Mann-Whitney U test: statistic = 972, P = 0.068, CCKC: Mann-Whitney U test: statistic = 103, P = 0.175 (E) Average responses of each cell type in the preceding 40 cm of the belt to the new reward location in the WT (left) and *Df(16)A*$^{+/-}$ (right) on Day 2. (F) Reward zone modulation index for all cells at the new reward zone on the first day of reward translocation. (AAC: Mann-Whitney U test: statistic = 132, P = 7.742e-4, PVBC: Mann-Whitney U test: statistic =460, P = 0.153, SomC: Mann-Whitney U test: statistic = 3460, P =0.049, IvC/NGFC: Mann-Whitney U test: statistic = 531, P = 0.254, CCKC: Mann-Whitney U test: statistic = 62, P = 0.409) (G) Proportion of positive place cells during reward translocation task. (Student's T-test: statistic = -0.4900, P = 0.6288). *n.s.* = not significant.

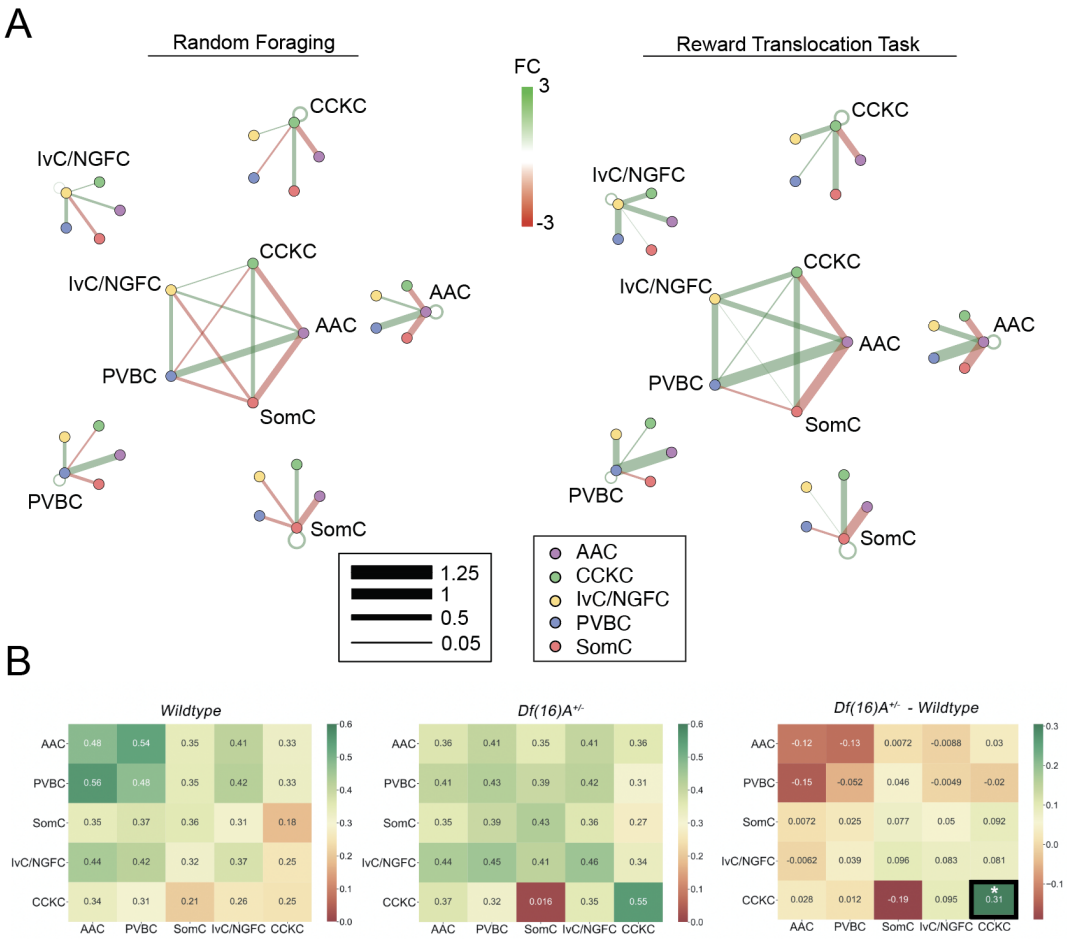

Supplemental Figure 6: (A) Circuit representation of the mean cell-to-cell-type interactions for each cell type by behavior paradigm (left: Random Foraging, right: Reward Translocation) in WT as determined by the probabilistic graphical model. Nodes represent different interneuron types, with colors corresponding to AAC (purple), CCKC (green), IvC/NGFC (blue), PVBC (yellow), and SomC (red). Edges connecting the nodes reflect the z-scores of the differences between the average correlations, with green edges indicating a correlation greater than expected by chance and red edges indicating less than expected. (B) Pairwise Pearson's correlation coefficient value matrix between cell types of ($\Delta F/F$) traces across the trial with velocity-driven activity regressed from the signal during the Random Foraging paradigm.

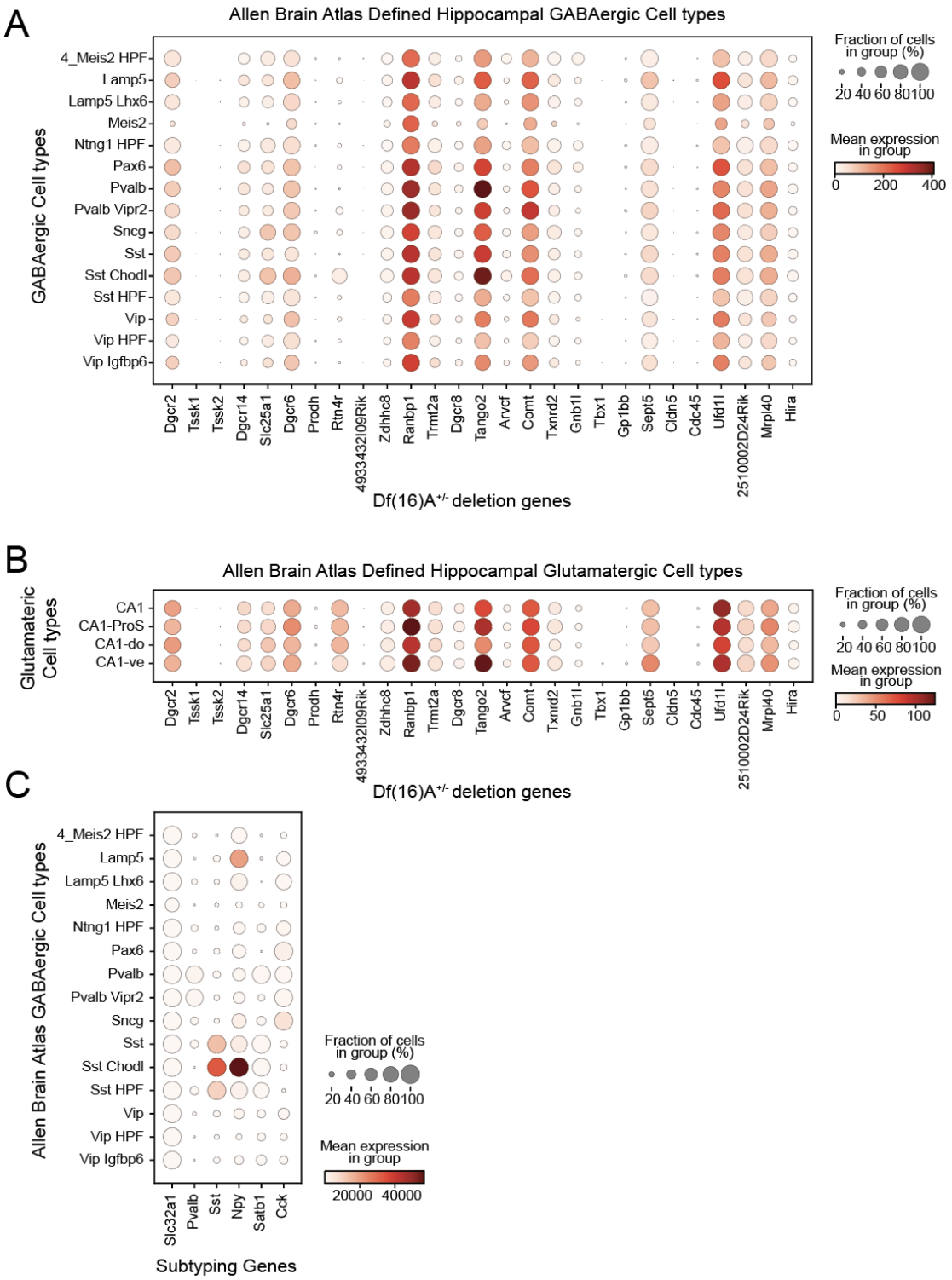

925 **Supplemental Figure 7:** Expression profile of genes residing within the deleted locus in *Df(16)A*$^{+/-}$ mice in defined hippocampal (A) GABAergic interneuron subtypes and (B) Glutamatergic subtypes from SMART-seq single cell RNAseq data from the Allen Brain Atlas[117]. (C) Expression profile of genes used for transgenic and immunohistochemical targeting for cell subtyping in Allen Brain Atlas defined hippocampal GABAergic cell-types.

References

1. Karayiorgou, M., Simon, T.J., and Gogos, J.A. (2010). 22q11.2 microdeletions: linking DNA structural variation to brain dysfunction and schizophrenia. Nature Reviews Neuroscience 2010 11:6 *11*, 402–416.

2. Jonas, R.K., Montojo, C.A., and Bearden, C.E. (2014). The 22q11.2 deletion syndrome as a window into complex neuropsychiatric disorders over the lifespan. Biol. Psychiatry *75*, 351–360.

3. Xu, B., Roos, J.L., Levy, S., van Rensburg, E.J., Gogos, J.A., and Karayiorgou, M. (2008). Strong association of de novo copy number mutations with sporadic schizophrenia. Nat. Genet. *40*, 880–885.

4. Marshall, C.R., Howrigan, D.P., Merico, D., Thiruvahindrapuram, B., Wu, W., Greer, D.S., Antaki, D., Shetty, A., Holmans, P.A., Pinto, D., et al. (2017). Contribution of copy number variants to schizophrenia from a genome-wide study of 41,321 subjects. Nat. Genet. *49*, 27–35.

5. Green, M., and Walker, E. (1985). Neuropsychological Performance and Positive and Negative Symptoms in Schizophrenia.

6. Bowie, C.R., Reichenberg, A., Patterson, T.L., Heaton, R.K., and Harvey, P.D. (2006). Determinants of real-world functional performance in schizophrenia subjects: Correlations with cognition, functional capacity, and symptoms. Am. J. Psychiatry *163*, 418–425.

7. Green, M.F. (2006). What are the functional consequences of neurocognitive deficits in schizophrenia? https://doi.org/10.1176/ajp.153.3.321 *153*, 321–330.

8. Aleman, A., Hijman, R., De Haan, E.H.F., and Kahn, R.S. (1999). Memory impairment in schizophrenia: A meta-analysis. Am. J. Psychiatry *156*, 1358–1366.

9. Danion, J.-M., Huron, C., and Vidailhet, P. (2007). Functional Mechanisms of Episodic Memory. Can. J. Psychiatry *52*, 693–701.

10. Fusar-Poli, P., Perez, J., Broome, M., Borgwardt, S., Placentino, A., Caverzasi, E., Cortesi, M., Veggiotti, P., Politi, P., Barale, F., et al. (2007). Neurofunctional correlates of vulnerability to psychosis: A systematic review and meta-analysis. Neurosci. Biobehav. Rev. *31*, 465–484.

11. Young, J.W., and Geyer, M.A. (2015). Developing treatments for cognitive deficits in schizophrenia: The challenge of translation. J. Psychopharmacol. *29*, 178–196.

12. Gogos, J.A., Crabtree, G., and Diamantopoulou, A. (2020). The abiding relevance of mouse models of rare mutations to psychiatric neuroscience and therapeutics. Schizophr. Res. *217*, 37–51.

13. Arguello, P.A., and Gogos, J.A. (2006). Modeling madness in mice: one piece at a time. Neuron *52*, 179–196.

14. Lisman, J. (2012). Excitation, inhibition, local oscillations, or large-scale loops: what causes the symptoms of schizophrenia? Curr. Opin. Neurobiol. *22*, 537–544.

15. Uhlhaas, P.J. (2013). Dysconnectivity, large-scale networks and neuronal dynamics in schizophrenia. Curr. Opin. Neurobiol. *23*, 283–290.

16. Krystal, J.H., Anticevic, A., Yang, G.J., Dragoi, G., Driesen, N.R., Wang, X.J., and Murray, J.D. (2017). Impaired Tuning of Neural Ensembles and the Pathophysiology of Schizophrenia: A Translational and Computational Neuroscience Perspective. Biol. Psychiatry *81*, 874–885.

17. Sigurdsson, T., Stark, K.L., Karayiorgou, M., Gogos, J.A., and Gordon, J.A. (2010). Impaired hippocampal–prefrontal synchrony in a genetic mouse model of schizophrenia. Nature *464*, 763–767.

18. Crabtree, G., and Gogos, J.A. (2014). Synaptic plasticity, neural circuits, and the emerging role of altered short-term information processing in schizophrenia. Front. Synaptic Neurosci. *6*. 10.3389/FNSYN.2014.00028.

19. Ferguson, B.R., and Gao, W.J. (2018). PV Interneurons: Critical Regulators of E/I Balance for Prefrontal Cortex-Dependent Behavior and Psychiatric Disorders. Front. Neural Circuits *12*. 10.3389/FNCIR.2018.00037.

20. Heckers, S., and Konradi, C. (2015). GABAergic mechanisms of hippocampal hyperactivity in schizophrenia. Schizophr. Res. *167*, 4–11.

21. Mukai, J., Cannavò, E., Sun, Z., Crabtree, G., and Diamantopoulou, A. (2019). Recapitulation and reversal of schizophrenia-related phenotypes in Setd1a - deficient mice.

22. Zaremba, J.D., Diamantopoulou, A., Danielson, N.B., Grosmark, A.D., Kaifosh, P.W., Bowler, J.C., Liao, Z., Sparks, F.T., Gogos, J.A., and Losonczy, A. (2017). Impaired hippocampal place cell dynamics in a mouse model of the 22q11.2 deletion. Nat. Neurosci. *20*, 1612–1623.

23. Mukai, J., Tamura, M., Fénelon, K., Rosen, A.M., Spellman, T.J., Kang, R., MacDermott, A.B., Karayiorgou, M., Gordon, J.A., and Gogos, J.A. (2015). Molecular substrates of altered axonal growth and brain connectivity in a mouse model of schizophrenia. Neuron *86*, 680–695.

24. Hamm, J.P., Peterka, D.S., Gogos, J.A., and Yuste, R. (2017). Altered Cortical Ensembles in Mouse Models of Schizophrenia. Neuron *94*, 153-167.e8.

25. Exposito-Alonso, D., and Rico, B. (2022). Mechanisms underlying circuit dysfunction in neurodevelopmental disorders. Annu. Rev. Genet. *56*, 391–422.

26. Farsi, Z., Nicolella, A., Simmons, S.K., Aryal, S., Shepard, N., Brenner, K., Lin, S., Herzog, L., Moran, S.P., Stalnaker, K.J., et al. (2023). Brain-region-specific changes in neurons and glia and dysregulation of dopamine signaling in Grin2a mutant mice. Neuron *111*, 3378-3396.e9.

27. Buzsáki, G., and Moser, E.I. (2013). Memory, navigation and theta rhythm in the hippocampal-entorhinal system. Nature Neuroscience 2013 16:2 *16*, 130–138.

28. O'Keefe, J., and Dostrovsky, J. (1971). The hippocampus as a spatial map. Preliminary evidence from unit activity in the freely-moving rat. Brain Res. *34*, 171–175.

29. Knierim, J.J., Lee, I., and Hargreaves, E.L. (2006). Hippocampal place cells: Parallel input streams, subregional processing, and implications for episodic memory. Hippocampus *16*, 755–764.

30. Danielson, N.B., Zaremba, J.D., Kaifosh, P., Bowler, J., Ladow, M., and Losonczy, A. (2016). Sublayer-Specific Coding Dynamics during Spatial Navigation and Learning in Hippocampal Area CA1. Neuron *91*, 652–665.

31. Hainmueller, T., and Bartos, M. (2018). Parallel emergence of stable and dynamic memory engrams in the hippocampus. Nature *558*, 292–296.

32. Mizuseki, K., Royer, S., Diba, K., and Buzsáki, G. (2012). Activity dynamics and behavioral correlates of CA3 and CA1 hippocampal pyramidal neurons. Hippocampus *22*, 1659–1680.

33. Rao-Ruiz, P., Couey, J.J., Marcelo, I.M., Bouwkamp, C.G., Slump, D.E., Matos, M.R., van der Loo, R.J., Martins, G.J., van den Hout, M., van IJcken, W.F., et al. (2019). Engram-specific transcriptome profiling of contextual memory consolidation. Nat. Commun. *10*, 1–14.

34. Rashid, T. (2005). Opposing gradients of ephrin-As and EphA7 in the superior colliculus are essential for topographic mapping in the mammalian visual system. Neuron *47*, 57–69.

35. Sosa, M., Gillespie, A.K., and Frank, L.M. (2018). Neural activity patterns underlying spatial coding in the hippocampus. Curr. Top. Behav. Neurosci. *37*, 43–100.

36. Ziv, Y., Burns, L.D., Cocker, E.D., Hamel, E.O., Ghosh, K.K., Kitch, L.J., Gamal, A.E., and Schnitzer, M.J. (2013). Long-term dynamics of CA1 hippocampal place codes. Nature Neuroscience 2013 16:3 *16*, 264–266.

37. Frank, L.M., Stanley, G.B., and Brown, E.N. (2004). Hippocampal Plasticity across Multiple Days of Exposure to Novel Environments. Journal of Neuroscience *24*, 7681–7689.

38. Hill, A.J. (1978). First occurrence of hippocampal spatial firing in a new environment. Exp. Neurol. *62*, 282–297.

39. Leutgeb, S., Leutgeb, J.K., Treves, A., Moser, M.B., and Moser, E.I. (2004). Distinct ensemble codes in hippocampal areas CA3 and CA1. Science *305*, 1295–1298.

40. Cacucci, F., Wills, T.J., Lever, C., Giese, K.P., and O'Keefe, J. (2007). Experience-Dependent Increase in CA1 Place Cell Spatial Information, But Not Spatial Reproducibility, Is Dependent on the Autophosphorylation of the α-Isoform of the Calcium/Calmodulin-Dependent Protein Kinase II. Journal of Neuroscience *27*, 7854–7859.

41. Karlsson, M.P., and Frank, L.M. (2008). Network Dynamics Underlying the Formation of Sparse, Informative Representations in the Hippocampus. Journal of Neuroscience *28*, 14271–14281.

42. Wilson, M.A., and McNaughton, B.L. (1993). Dynamics of the hippocampal ensemble code for space. Science *261*, 1055–1058.

43. Turi, G.F., Li, W.-K., Chavlis, S., Pandi, I., Hare, J.O., Priestley, J.B., Grosmark, A.D., Liao, Z., Ladow, M., Zhang, J.F., et al. (2019). Vasoactive Intestinal Polypeptide-Expressing Interneurons in the Hippocampus Support Goal-Article Vasoactive Intestinal Polypeptide-Expressing Interneurons in the Hippocampus Support Goal-Oriented Spatial Learning. Neuron, 1–16.

44. Gauthier, J.L., and Tank, D.W. (2018). A Dedicated Population for Reward Coding in the Hippocampus. Neuron *99*, 179-193.e7.

45. Hollup, S.A., Molden, S., Donnett, J.G., Moser, M.B., and Moser, E.I. (2001). Accumulation of Hippocampal Place Fields at the Goal Location in an Annular Watermaze Task. Journal of Neuroscience *21*, 1635–1644.

46. Muller, R.U., and Kubie, J.L. (1987). The effects of changes in the environment on the spatial firing of hippocampal complex-spike cells. Journal of Neuroscience *7*, 1951–1968.

47. Colgin, L.L., Moser, E.I., and Moser, M.B. (2008). Understanding memory through hippocampal remapping. Trends Neurosci. *31*, 469–477.

48. Kubie, J.L., Levy, E.R.J., and Fenton, A.A. (2020). Is hippocampal remapping the physiological basis for context? Hippocampus *30*, 851.

49. Kepecs, A., and Fishell, G. (2014). Interneuron cell types are fit to function. Nature *505*, 318–326.

50. Tzilivaki, A., Tukker, J.J., Maier, N., Poirazi, P., Sammons, R.P., and Schmitz, D. (2023). Hippocampal GABAergic interneurons and memory. Neuron *111*, 3154–3175.

51. Cardin, J.A. (2018). Inhibitory interneurons regulate temporal precision and correlations in cortical circuits. Trends Neurosci. *41*, 689–700.

52. Harris, K.D., Hochgerner, H., Skene, N.G., Magno, L., Katona, L., Gonzales, C.B., Somogyi, P., Kessaris, N., Linnarsson, S., Hjerling-leffler, J., et al. (2018). Classes and continua of hippocampal CA1 inhibitory neurons revealed by single-cell transcriptomics.

53. Pelkey, K.A., Chittajallu, R., Craig, M.T., Tricoire, L., Wester, J.C., and Mcbain, X.C.J. (2017). Hippocampal GABAergic inhibitory interneurons. Physiol. Rev. *97*, 1619–1747.

54. Freund, T.F., and Buzsáki, G. (1996). Interneurons of the Hippocampus. Hippocampus *6*, 347–470.

55. Dudok, B., Szoboszlay, M., Paul, A., Klein, P.M., Liao, Z., Hwaun, E., Szabo, G.G., Geiller, T., Vancura, B., Wang, B.-S., et al. (2021). Recruitment and inhibitory action of hippocampal axo-axonic cells during behavior. Neuron *109*, 3838-3850.e8.

56. Dudok, B., Klein, P.M., Hwaun, E., Lee, B.R., Yao, Z., Fong, O., Bowler, J.C., Terada, S., Sparks, F.T., Szabo, G.G., et al. (2021). Alternating sources of perisomatic inhibition during behavior. Neuron *109*, 997-1012.e9.

57. Chamberland, S., Grant, G., Machold, R., Nebet, E.R., Tian, G., Stich, J., Hanani, M., Kullander, K., and Tsien, R.W. (2024). Functional specialization of hippocampal somatostatin-expressing interneurons. Proc. Natl. Acad. Sci. U. S. A. *121*, e2306382121.

58. Varga, C., Golshani, P., and Soltesz, I. (2012). Frequency-invariant temporal ordering of interneuronal discharges during hippocampal oscillations in awake mice. Proc. Natl. Acad. Sci. U. S. A. *109*, E2726-34.

59. Somogyi, P., and Klausberger, T. (2005). Defined types of cortical interneurone structure space and spike timing in the hippocampus. J. Physiol. *562*, 9–26.

60. Grienberger, C., Milstein, A.D., Bittner, K.C., Romani, S., and Magee, J.C. (2017). Inhibitory suppression of heterogeneously tuned excitation enhances spatial coding in CA1 place cells. Nat. Neurosci. *20*, 417–426.

61. Juarez, P., and Martínez Cerdeño, V. (2022). Parvalbumin and parvalbumin chandelier interneurons in autism and other psychiatric disorders. Front. Psychiatry *13*, 913550.

62. Beasley, C.L., and Reynolds, G.P. (1997). Parvalbumin-immunoreactive neurons are reduced in the prefrontal cortex of schizophrenics. Schizophr. Res. *24*, 349–355.

63. Lewis, D.A., Curley, A.A., Glausier, J.R., and Volk, D.W. (2012). Cortical parvalbumin interneurons and cognitive dysfunction in schizophrenia. Preprint, 10.1016/j.tins.2011.10.004 10.1016/j.tins.2011.10.004.

64. Nakazawa, K., Zsiros, V., Jiang, Z., Nakao, K., Kolata, S., Zhang, S., and Belforte, J.E. (2012). GABAergic interneuron origin of schizophrenia pathophysiology. Neuropharmacology *62*, 1574–1583.

65. Chung, D.W., Fish, K.N., and Lewis, D.A. (2016). Pathological basis for deficient excitatory drive to cortical parvalbumin interneurons in schizophrenia. Am. J. Psychiatry *173*, 1131–1139.

66. Fung, S.J., Fillman, S.G., Webster, M.J., and Shannon Weickert, C. (2014). Schizophrenia and bipolar disorder show both common and distinct changes in cortical interneuron markers. Schizophr. Res. *155*, 26–30.

67. Gonzalez-Burgos, G., Cho, R.Y., and Lewis, D.A. (2015). Alterations in Cortical Network Oscillations and Parvalbumin Neurons in Schizophrenia. Biol. Psychiatry *77*, 1031–1040.

68. Lewis, D.A. (2014). Inhibitory neurons in human cortical circuits: substrate for cognitive dysfunction in schizophrenia. Curr. Opin. Neurobiol. *26*, 22–26.

69. Dienel, S.J., Dowling, K.F., Barile, Z., Bazmi, H.H., Liu, A., Vespoli, J.C., Fish, K.N., and Lewis, D.A. (2023). Diagnostic specificity and association with cognition of molecular alterations in prefrontal somatostatin neurons in schizophrenia. JAMA Psychiatry *80*, 1235–1245.

70. Dienel, S.J., Fish, K.N., and Lewis, D.A. (2023). The nature of prefrontal cortical GABA neuron alterations in schizophrenia: Markedly lower somatostatin and parvalbumin gene expression without missing neurons. Am. J. Psychiatry *180*, 495–507.

71. Geiller, T., Vancura, B., Terada, S., Troullinou, E., Chavlis, S., Tsagkatakis, G., Tsakalides, P., Ócsai, K., Poirazi, P., Rózsa, B.J., et al. (2020). Large-Scale 3D Two-Photon Imaging of Molecularly Identified CA1 Interneuron Dynamics in Behaving Mice. Neuron *108*, 968-983.e9.

72. Vancura, B., Geiller, T., Grosmark, A., Zhao, V., and Losonczy, A. (2023). Inhibitory control of sharp-wave ripple duration during learning in hippocampal recurrent networks. Nat. Neurosci. *26*, 788–797.

73. Mukherjee, A., Carvalho, F., Eliez, S., and Caroni, P. (2019). Long-Lasting Rescue of Network and Cognitive Dysfunction in a Genetic Schizophrenia Model. Cell *178*, 1387-1402.e14.

74. Geiller, T., Sadeh, S., Rolotti, S.V., Blockus, H., Vancura, B., Negrean, A., Murray, A.J., Rózsa, B., Polleux, F., Clopath, C., et al. (2021). Local circuit amplification of spatial selectivity in the hippocampus. Nature *601*, 105–109.

75. Rolotti, S.V., Ahmed, M.S., Szoboszlay, M., Geiller, T., Negrean, A., Blockus, H., Gonzalez, K.C., Sparks, F.T., Solis Canales, A.S., Tuttman, A.L., et al. (2022). Local feedback inhibition tightly controls rapid formation of hippocampal place fields. Neuron *110*, 783-794.e6.

76. Hangya, B., Li, Y., Muller, R.U., and Czurkó, A. (2010). Complementary spatial firing in place cell-interneuron pairs. J. Physiol. *588*, 4165–4175.

77. Ego-Stengel, V., and Wilson, M.A. (2007). Spatial selectivity and theta phase precession in CA1 interneurons. Hippocampus *17*, 161–174.

78. Markus, E.J., Barnes, C.A., McNaughton, B.L., Gladden, V.L., and Skaggs, W.E. (1994). Spatial information content and reliability of hippocampal CA1 neurons: effects of visual input. Hippocampus *4*, 410–421.

79. Skaggs, W., McNaughton, B., and Gothard, K. (1992). An information-theoretic approach to deciphering the hippocampal code. Adv. Neural Inf. Process. Syst., 1030–1037.

80. Grijseels, D.M., Shaw, K., Barry, C., and Hall, C.N. (2021). Choice of method of place cell classification determines the population of cells identified. PLoS Comput. Biol. *17*, e1008835.

81. Stark, K.L., Xu, B., Bagchi, A., Lai, W.S., Liu, H., Hsu, R., Wan, X., Pavlidis, P., Mills, A.A., Karayiorgou, M., et al. (2008). Altered brain microRNA biogenesis contributes to phenotypic deficits in a 22q11-deletion mouse model. Nat. Genet. *40*, 751–760.

82. Diamantopoulou, A., Sun, Z., Mukai, J., Xu, B., Fenelon, K., Karayiorgou, M., and Gogos, J.A. (2017). Loss-of-function mutation in *Mirta22/Emc10* rescues specific schizophrenia-related phenotypes in a mouse model of the 22q11.2 deletion. Proc. Natl. Acad. Sci. U. S. A. *114*, E6127–E6136.

83. Marissal, T., Salazar, R.F., Bertollini, C., Mutel, S., De Roo, M., Rodriguez, I., Müller, D., and Carleton, A. (2018). Restoring wild-type-like CA1 network dynamics and behavior during adulthood in a mouse model of schizophrenia. Nat. Neurosci. *21*, 1412–1420.

84. Forro, T., and Klausberger, T. (2023). Differential behavior-related activity of distinct hippocampal interneuron types during odor-associated spatial navigation. Neuron *111*, 2399-2413.e5.

85. Michon, F.-X., Laplante, I., Bosson, A., Robitaille, R., and Lacaille, J.-C. (2023). mTORC1-mediated acquisition of reward-related representations by hippocampal somatostatin interneurons. Mol. Brain *16*, 55.

86. Schneider, A., Azabou, M., McDougall-Vigier, L., Parks, D.F., Ensley, S., Bhaskaran-Nair, K., Nowakowski, T., Dyer, E.L., and Hengen, K.B. (2023). Transcriptomic cell type structures in vivo neuronal activity across multiple timescales. Cell Rep. *42*, 112318.

87. Somogyi, J., Baude, A., Omori, Y., Shimizu, H., El Mestikawy, S., Fukaya, M., Shigemoto, R., Watanabe, M., and Somogyi, P. (2004). GABAergic basket cells expressing cholecystokinin contain vesicular glutamate transporter type 3 (VGLUT3) in their synaptic terminals in hippocampus and isocortex of the rat. Eur. J. Neurosci. *19*, 552–569.

88. Fuhrmann, F., Justus, D., Sosulina, L., Kaneko, H., Beutel, T., Friedrichs, D., Schoch, S., Schwarz, M.K., Fuhrmann, M., and Remy, S. (2015). Locomotion, theta oscillations, and the speed-correlated firing of hippocampal neurons are controlled by a medial septal glutamatergic circuit. Neuron *86*, 1253–1264.

89. Arriaga, M., and Han, E.B. (2017). Dedicated hippocampal inhibitory networks for locomotion and immobility. J. Neurosci. *37*, 9222–9238.

90. Lapray, D., Lasztoczi, B., Lagler, M., Viney, T.J., Katona, L., Valenti, O., Hartwich, K., Borhegyi, Z., Somogyi, P., and Klausberger, T. (2012). Behavior-dependent specialization of identified hippocampal interneurons. Nat. Neurosci. *15*, 1265–1271.

91. Gridchyn, I., Schoenenberger, P., O'Neill, J., and Csicsvari, J. (2020). Optogenetic inhibition-mediated activity-dependent modification of CA1 pyramidal-interneuron connections during behavior. Elife *9*. 10.7554/eLife.61106.

92. Schoenenberger, P., O'Neill, J., and Csicsvari, J. (2016). Activity-dependent plasticity of hippocampal place maps. Nat. Commun. *7*, 11824.

93. Priestley, J.B., Bowler, J.C., Rolotti, S.V., Fusi, S., and Losonczy, A. (2022). Signatures of rapid plasticity in hippocampal CA1 representations during novel experiences. Neuron *110*, 1978-1992.e6.

94. Hainmueller, T., Cazala, A., Huang, L.-W., and Bartos, M. (2024). Subfield-specific interneuron circuits govern the hippocampal response to novelty in male mice. Nat. Commun. *15*, 714.

95. Rangel Guerrero, D.K., Balueva, K., Barayeu, U., Baracskay, P., Gridchyn, I., Nardin, M., Roth, C.N., Wulff, P., and Csicsvari, J. (2024). Hippocampal cholecystokinin-expressing interneurons regulate temporal coding and contextual learning. Neuron. 10.1016/j.neuron.2024.03.019.

96. Lovett-Barron, M., Kaifosh, P., Kheirbek, M.A., Danielson, N., Zaremba, J.D., Reardon, T.R., Turi, G.F., Hen, R., Zemelman, B.V., and Losonczy, A. (2014). Dendritic inhibition in the hippocampus supports fear learning. Science *343*, 857–863.

97. Varga, V., Losonczy, A., Zemelman, B.V., Borhegyi, Z., Nyiri, G., Domonkos, A., Hangya, B., Holderith, N., Magee, J.C., and Freund, T.F. (2009). Fast synaptic subcortical control of hippocampal circuits. Science *326*, 449–453.

98. Basu, J., Zaremba, J.D., Cheung, S.K., Hitti, F.L., Zemelman, B.V., Losonczy, A., and Siegelbaum, S.A. (2016). Gating of hippocampal activity, plasticity, and memory by entorhinal cortex long-range inhibition. Science *351*, aaa5694.

99. Chamberland, S., and Topolnik, L. (2012). Inhibitory control of hippocampal inhibitory neurons. Front. Neurosci. *0*, 165.

100. Szabo, G.G., Farrell, J.S., Dudok, B., Hou, W.-H., Ortiz, A.L., Varga, C., Moolchand, P., Gulsever, C.I., Gschwind, T., Dimidschstein, J., et al. (2022). Ripple-selective GABAergic projection cells in the hippocampus. Neuron *110*, 1959-1977.e9.

101. Batista-Brito, R., Vinck, M., Ferguson, K.A., Chang, J.T., Laubender, D., Lur, G., Mossner, J.M., Hernandez, V.G., Ramakrishnan, C., Deisseroth, K., et al. (2017). Developmental Dysfunction of VIP Interneurons Impairs Cortical Circuits. Neuron *95*, 884-895.e9.

102. Piskorowski, R.A., Nasrallah, K., Diamantopoulou, A., Mukai, J., Hassan, S.I., Siegelbaum, S.A., Gogos, J.A., and Chevaleyre, V. (2016). Age-Dependent Specific Changes in Area CA2 of the Hippocampus and Social Memory Deficit in a Mouse Model of the 22q11.2 Deletion Syndrome. Neuron *89*, 163–176.

103. Brown, J.A., Ramikie, T.S., Schmidt, M.J., Báldi, R., Garbett, K., Everheart, M.G., Warren, L.E., Gellért, L., Horváth, S., Patel, S., et al. (2015). Inhibition of parvalbumin-expressing interneurons results in complex behavioral changes. Mol. Psychiatry *20*, 1499–1507.

104. Sauer, J.-F., and Bartos, M. (2022). Disrupted-in-schizophrenia-1 is required for normal pyramidal cell-interneuron communication and assembly dynamics in the prefrontal cortex. Elife *11*. 10.7554/eLife.79471.

105. Del Pino, I., García-Frigola, C., Dehorter, N., Brotons-Mas, J.R., Alvarez-Salvado, E., Martínez de Lagrán, M., Ciceri, G., Gabaldón, M.V., Moratal, D., Dierssen, M., et al. (2013). Erbb4 deletion from fast-spiking interneurons causes schizophrenia-like phenotypes. Neuron *79*, 1152–1168.

106. Schmidt, M.J., Horvath, S., Ebert, P., Norris, J.L., Seeley, E.H., Brown, J., Gellert, L., Everheart, M., Garbett, K.A., Grice, T.W., et al. (2013). Modulation of behavioral networks by selective interneuronal inactivation. Molecular Psychiatry 2013 19:5 *19*, 580–587.

107. Starc, M., Murray, J.D., Santamauro, N., Savic, A., Diehl, C., Cho, Y.T., Srihari, V., Morgan, P.T., Krystal, J.H., Wang, X.J., et al. (2017). Schizophrenia is associated with a pattern of spatial working memory deficits consistent with cortical disinhibition. Schizophr. Res. *181*, 107–116.

108. Morris, H.M., Hashimoto, T., and Lewis, D.A. (2008). Alterations in Somatostatin mRNA Expression in the Dorsolateral Prefrontal Cortex of Subjects with Schizophrenia or Schizoaffective Disorder. Cereb. Cortex *18*, 1575–1587.

109. Morris, H.M., Stopczynski, R.E., and Lewis, D.A. (2009). NPY mRNA expression in the prefrontal cortex: Selective reduction in the superficial white matter of subjects with schizoaffective disorder. Schizophr. Res. *115*, 261–269.

110. Koukouli, F., Rooy, M., Tziotis, D., Sailor, K.A., O'Neill, H.C., Levenga, J., Witte, M., Nilges, M., Changeux, J.P., Hoeffer, C.A., et al. (2017). Nicotine reverses hypofrontality in animal models of addiction and schizophrenia. Nature Medicine 2017 23:3 *23*, 347–354.

111. Rocco, B.R., DeDionisio, A.M., Lewis, D.A., and Fish, K.N. (2017). Alterations in a Unique Class of Cortical Chandelier Cell Axon Cartridges in Schizophrenia. Biol. Psychiatry *82*, 40–48.

112. Wang, Y., Zhang, P., and Wyskiel, D.R. (2016). Chandelier Cells in Functional and Dysfunctional Neural Circuits. Front. Neural Circuits *10*, 33.

113. Van Derveer, A.B., Bastos, G., Ferrell, A.D., Gallimore, C.G., Greene, M.L., Holmes, J.T., Kubricka, V., Ross, J.M., and Hamm, J.P. (2021). A role for somatostatin-positive interneurons in neuro-oscillatory and information processing deficits in schizophrenia. Schizophr. Bull. *47*, 1385–1398.

114. Mancini, V., Saleh, M.G., Delavari, F., Bagautdinova, J., and Eliez, S. (2023). Excitatory/inhibitory imbalance underlies hippocampal atrophy in individuals with 22q11.2 deletion syndrome with psychotic symptoms. Biol. Psychiatry *94*, 569–579.

115. Liu, Y., Ouyang, P., Zheng, Y., Mi, L., Zhao, J., Ning, Y., and Guo, W. (2021). A selective review of the excitatory-inhibitory imbalance in schizophrenia: Underlying biology, genetics, microcircuits, and symptoms. Front. Cell Dev. Biol. *9*, 664535.

116. Kaifosh, P., Zaremba, J.D., Danielson, N.B., and Losonczy, A. (2014). SIMA: Python software for analysis of dynamic fluorescence imaging data. Front. Neuroinform. *8*, 80.

117. Yao, Z., Nguyen, T.N., van Velthoven, C.T.J., Goldy, J., Sedeno-Cortes, A.E., and Fahimeh Baftizadeh1 Darren Bertagnolli1 Tamara Casper1 Kirsten Crichton1 Song-Lin Ding1 Olivia Fong1 Emma Garren1 Alexandra Glandon1 James Gray1 Lucas T. Graybuck1 Daniel Hirschstein1 Matthew Kroll1 Kanan Lathia1 Boaz Levi1 Delissa McMillen1, H.Z. (2020). A taxonomy of transcriptomic cell types across the isocortex and hippocampal formation. bioRxiv. 10.1101/2020.03.30.015214.